Title
FRACTURE TOUGHNESS OF ALUMINUM ALLOYS UNDER CORROSIVE CONDITIONS

Author
Wood, William E.

Publication Date
1970-09-01

UCRL-19676
c.2

FRACTURE TOUGHNESS OF ALUMINUM ALLOYS UNDER CORROSIVE CONDITIONS

William E. Wood
(M. S. Thesis)

September 1970

AEC Contract No. W-7405-eng-48

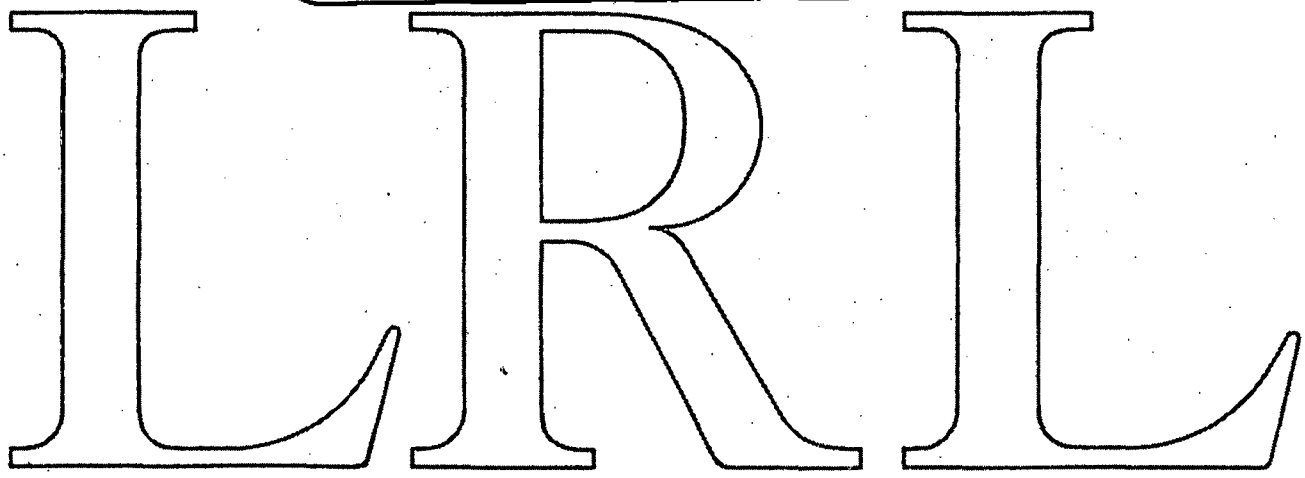

LAWRENCE RADIATION LABORATORY
UNIVERSITY of CALIFORNIA BERKELEY

UCRL-19676
c.2

25

DISCLAIMER

Contents

LIST OF SYMBOLS

K	stress intensity parameter, psi-in 1/2
B	specimen thickness, in.
W	specimen width, in.
a	1/2 crack length, in.
E	Young's modulus, psi
P	applied load, lbs.
T	temperature, ^{o}Kelvin
g	acceleration, ft/sec^2
e	length between load points, in.
t	time, min.
ℓ_c	amount of stress corrosion dissolution between mechanical jumps
ℓ_j	amount of one mechanical jump, in.
$(\Delta t)_s$	time between stress waves, sec.
σ_{ys}	yield strength at 0.2% offset, psi.
Q	activation energy, cal/mole
R	universal gas constant
c_1	constant
g	amplitude of the stress waves, ft/sec^2
ΔA	increment of area swept out by the advancing crack, in^2
Δw	width of a discontinuous jump, in.
A	constant

I. INTRODUCTION

The problem of stress corrosion cracking is a serious and complicated one in the development of many new materials and equipment. It becomes even more serious as the trend to higher strength to weight ratios increases, as for example in the aircraft industry. Also in the chemical industry stress corrosion cracking is always a threat with the presence of pressurized containers and tubing used for the making, storing, and transportation of chemicals. Furthermore, stress corrosion cracks can propagate without externally applied loads. The internal stresses from welding, forming, or machining can be serious enough to cause cracking, and once started a crack can be driven without any applied or residual stress, by just the presence of corrosion products.

The need for high strength light weight materials in the aircraft industry has led to many investigations into the mechanisms of stress corrosion cracking of aluminum alloys. However, no unified theory has yet been accepted which explains SCC of high strength aluminum alloys.

The primary objective of this investigation was to examine the nature of slow crack growth in the 7075-T6 aluminum alloy under the combined action of an applied stress and corrosive environment. The first step was to try to observe any discontinuous crack growth by the use of stress wave emission techniques, then to investigate the crack growth rate as a function of temperature and stress intensity. To do this a testing program was set up whereby (1) the SEN fracture specimens could be loaded to different stress intensity

levels; (2) the temperature of the test environment could be closely controlled; and (3) the acoustic emission of stress waves resulting from discontinuous crack growth could be monitored.

This investigation has shown the nature of slow crack growth in the 7075-T6 aluminum alloy, when subjected to both a stress and corrosive environment.

II. MATERIAL

A commerical precipitation hardening aluminum alloy, designated 7075, obtained as rolled sheet .080 in. thick and tempered to the -T6 condition, was selected for this study. The -T6 temper refers to a solution heat treated and artificially aged condition. The commercially specified composition[1] is 5.6% Zn, 2.5% Mg, 1.6% Cu and 0.30% Cr, 0.7% Fe, 0.5% Si, 0.3% Mn, 0.2% Ti.

III. MATERIAL PREPARATION

A. Cold working and heat treatment

In an effort to increase the grain size of the material through subsequent heat treatment, it was first cold rolled to .060 in. thickness, (25% reduction, the rolling direction was perpendicular to the grain orientation of the material). Next the plate was solution heat treated at 937°F ±2°F for three days, and then immediately quenched in water at 180°F, resulting in a cooling rate of about 150°F per second.[2] The material was then aged for five days at 190°F to a -T6 temper. This aging process has been reported by Gruhl[3] as leading to an increased susceptibility to stress corrosion cracking.

B. Tensile and fracture testing specimens

Standard uniaxial tensile specimens[4] were machined with 1.0 in. gage lengths and 0.125 in. widths. The tensile axis was parallel to the grain orientation of the sheet, Fig. 2.

Single edge notched fracture specimens were machined with their tensile axis perpendicular to the grain orientation of the sheet,

Fig. 1. The specimen geometry selected has been given by Brown and Srawley.[5] The SEN specimens were pre-fatigue cracked in a tension-tension fatigue machine to introduce a crack with a very sharp notch-tip radius.

IV. EXPERIMENTAL PROCEDURE

A. Program

Since, to detect discontinuous intergranular crack growth, a large grain size is desirable, and since the specimen thickness is proportional to the discontinuous crack growth, preliminary work was done to determine the optimum combination of sheet thickness, cold working, and heat treatment conditions which would produce the thickest specimens possible with a suitable grain size.

To verify the properties of the as received material and the cold worked and heat treated material, standard tensile tests were performed. To measure the slow crack growth rate as a function of stress intensity, tests were run over a stress intensity range of 9,250 psi-in.$^{1/2}$ to 49,600 psi-in.$^{1/2}$. To measure the crack growth rate as a function of environmental temperature, tests were performed at three different average stress intensity levels over a temperature range from 10°C to 73°C. For all tests the slow crack growth was monitored using stress wave emission techniques. Scanning electron microscope studies were done to correlate fracture appearance and characteristics with the test results.

B. Tensile and fracture tests

Uniaxial tensile tests were performed at room temperature on a 5000 kg Instron machine using a crosshead speed of .008 in./min.. The SEN fracture tests were also done on the same machine using a crosshead speed of .02 in./min. to load the specimens for tests done at room temperature, and .04 in./min. for tests done at elevated temperatures. Fig. 11 shows an actual SEN specimen.

C. Test environment

The stress corrosion cracking tests using the SEN specimens were done in a 3.5% NaCl solution with $AlCl_3$ added to lower the pH of the solution to less than 2. In order to determine the crack growth rate as a function of temperature, the NaCl + $AlCl_3$ solution was heated to a controlled temperature, and then allowed to flow slowly through a plastic tubing and past the notched area of the SEN specimen, as illustrated in Fig. 3. A thermometer was inserted into the tubing close to the specimen in order to actually measure the temperature of the solution as it passed the specimen. Fig. 4 shows the actual placement of the tubing around the SEN specimen.

D. Stress wave emission technique

Elastic stress waves are caused by the discontinuous growth of a crack before catastrophic failure. By using a suitable piezo-electric transducer attached to the specimen grips, these emissions can be detected, if they are within the sensitivity range of the instrument. The stress wave emission technique developed by Hartbower

et al[6-8] was used to study the behavior of slow crack growth propagation in SEN specimens, and provides an extremely sensitive method for monitoring acoustic emissions produced by discontinuous crack growth.

The instrumentation is shown schematically in Fig. 3. Figs. 4 and 5 show the actual test setup used to monitor and record the signal. As this signal is the result of a very small amount of energy being released by a discontinuous crack movement, it is necessary to amplify it and to filter out extraneous noise. An Endevco accelerometer, model 2234E, was used for the piezoelectric transducer and had a sensitivity of 59.4 picocoulombs/g and a major resonant frequency of 32 KHz. The signal from the accelerometer was first amplified 150 times by a charge amplifier, at a gain of 1 g. The gain was then increased 250 times by a voltage amplifier. The amplified signal was then passed through a band pass filter with a low pass of 200 KHz and a high pass of 3 KHz. The filtered signal was then fed in parallel to an Ampex recorder with a maximum frequency response of 40 KHz at 15 ips, and also into the oscilloscope for observation. After the test was over the taped signal was played back at 7-1/2 ips (at one half speed and thus one half of the highest recorded frequency), so as to be within the frequency response of the galvonometer (5 KHz). The resulting gain of the system comprising the charge amplifier, voltage amplifier, and the recorder amplifier of 1 to 3, was approximately 112,500. With this test setup many tests could be run in succession, recorded on tape and also on the visicorder strip chart, model 1108.

E. Microscopy

(1) Metallography: Standard metallographic techniques were used to examine the microstructure of the as-received material in comparison to the cold work and heat treated material. Figure 12 shows the microstructures which were used to estimate the number of grains per unit thickness. Also, Fig. 14 shows the side view of a SEN specimen which has been tested and the pieces fitted together again. All the tested specimens were similarly examined to be sure that there was only one active crack path for each test.

The metallography was done on pieces sectioned from the SEN specimens wet ground in successive stages to a 600 grit paper, polished on a diamond wheel to a 0.25 micron finish, and finally micropolished on a syntron wheel in a solution of distilled water and 0.05 micron alumina. A dilute keller's etch was used to etch the specimens.

(2) Fractography: The scanning electron microscope (SEM) employing secondary electron emission at 25 KV was used to study the fracture surface of the specimens over a range of magnification from 200X to 20,000X. The fracture surfaces selected show the effect of temperature and stress intensity on the morphology of the fracture surface.

Because of the large depth of field associated with the SEM, it was possible to characterize the morphology of the fracture surface, and to estimate the amount of dimpled rupture as a function of stress intensity.

V. EXPERIMENTAL RESULTS AND OBSERVATIONS

A. Materials

The as received material contained about 120 grains across the thickness, or a grain width of about 12.5 microns. After cold rolling and heat treating there were about 60 grains across the thickness or a grain width of about 25 microns. The grain length did not change between the two conditions and averaged about 100 microns. Table II shows that there was a decrease in strength and hardness while the elongation increased slightly over the as received material.

B. Slow crack growth rate

(1) Effect of stress intensity: Starting with a pre-fatigue cracked SEN speciman, the general formula for expressing K_1 has been given by Brown and Srawley[5] as

$$K = Y \frac{P}{B} \frac{a^{1/2}}{W}$$

where $Y = F(a/w)$ is the correction factor for finite width and crack geometry. For the SEN specimen they proposed that

$$Y = 1.99 - 0.41\,(a/w) + 18.70\,(a/w)^2 - 38.48\,(a/w)^3 + 58.85\,(a/w)^4$$

Fig. 6 shows a log-log plot of the stress intensity versus the slow crack growth rate. The slope of the curve, determined by a least square analysis on an IBM computer, was found to be equal to 2. No crack growth was observed (after 328 minutes) at a stress intensity of 9250 psi-$in^{1/2}$. Due to the geometry of the SEN specimen, the

stress intensity level increases as the crack grows. Thus for these tests the initial value, K_i, and the final value, K_f, were calculated and an average value assumed. In order that there be only a small change in the stress intensity during the test, the tests were run long enough so that there would be a relatively small amount of crack growth. The specimens were then broken by loading at .13 in./min. so that the amount of slow crack growth could be determined (Fig. 13).

(2) Effect of environmental temperature: Tests were performed to determine the dependence of the slow crack growth rate on the temperature of the environment. The results are shown in Figs. 7, 8, and 9 for three different stress intensity levels. Again, a least squares analysis was done to determine the best curves that could be drawn through the data points. Fig. 10 shows the superimposed curves, and the effect of increasing the stress intensity on the crack growth rate for any given temperature. From the equation

$$\frac{da}{dt} = Ae^{\frac{-Q}{RT}}$$

the activation energy, Q, can be computed from the slope of the curves. The calculated values are listed with each curve. The average value of the apparent activation energy was 11,200 cal/mole.

C. Stress wave emission observations and results

Stress wave activity was observed in all the tests where slow crack growth occurred. Figs. 28 through 33 show some representative oscillogram recordings of the monitored waves. Table III shows the dependence of the amplitude and frequency of the stress waves on the stress intensity. Due to the sensitivity of the system, the bubbles forming by the reaction of the environment with the material, produced a noise, which at elevated temperatures made it impossible to distinguish between real stress waves and the wave produced by the bubbles. Even at 48°C the noise of the bubbles made it impossible to identify the stress waves. However, at 33°C and below, bubbles did not significantly raise the background noise, and allowed stress waves to be observed as a function of stress intensity, Fig. 28. Figs. 30 and 31 compare background noise with actual tests run at the same temperatures. Fig. 32 shows background noise as a function of temperature only. Fig. 29 compares a test done in air to a test done in the environment at the same temperature and stress intensity level.

The number of stress waves per sec. taken from data stored on the tapes, in only of the major waves. The real SWE activity might possibly be very much higher, involving many more low energy waves. The average amplitude of the stress waves for each test was obtained from the amplitude of the six biggest waves in a given time interval.

Qualitatively then, the SWE observations show that as the stress intensity increases, the frequency and amplitude of the stress waves increases. Estimates of the incremental area swept out by the crack have been made by Gerberich and Hartbower.[6]

Quantitatively, a relationship between the incremental crack growth and stress wave activity has been suggested by Gerberich[9]. Based on experimental work on an Al-Zn alloy, he derived a semi-empirical relationship of the form

$$g = \frac{2\Delta A \cdot K^2}{C_1 E e}$$

where g is proportional to the amplitude of a stress wave, ΔA is the incremental area swept out by one stress wave, e is the distance between loading pins, C is a constant, and E is Young's modulus. By carefully calibrating the instruments shown schematically in Fig. 3, the amplitude of the stress waves can be expressed in terms of g. For the settings used in these tests a stress wave amplitude of 1.9 in. is equal to .0008 g. Table III shows the calculated values of ΔA for different stress intensity levels based on this equation.

D. Fracture surface observations

Fig. 13 shows representative macroscopic fracture features for all the tests. Indicated on the figures is the pre-fatigue cracked region (A-B), the slow crack growth region (B-C), and the unstable crack growth region (C-D). Figs.15 through 27 show the microscopie details of the fracture surfaces. At low temperatures, the time of the tests was longer, meaning that the solution was in contact with the fracture surface for longer periods of time, thus destroying many of the fine details. This made it difficult to find any areas of dimpled rupture that might have been present initially.

However, at high temperatures with shorter exposure times to the environment, fine detail can be observed. A comparison of Figs. 21-A and 20-A shows that as the stress intensity level increases, the amount of dimpled rupture also increases. The dimpled regions represent discontinuous jumping or tearing of the material, as compared with the relatively flat surfaces which indicate a continuous crack movement due to chemical dissolution, an electrochemical process.

Fig. 26 shows a residue of the test solution. The features are perfectly smooth with no texture present as in the actual material. The cracks in the residue are formed as the solution dries, shrinking and cracking. Fig. 27 clearly shows some regions containing residual deposits of the solution and the difference in appearance between the residual solution and the actual test material.

E. Stress intensity factor and the size of the discontinuous crack jump

An expression can be written for the crack growth rate in terms of a crack movement with two associated components: ℓ_j, the amount of the forward crack advance due to a mechanical jump, and ℓ_c, the amount of the forward crack advance due to electrochemical dissolution in between discontinuous jumps.

$$\left(\frac{da}{dt}\right)_T = \frac{\ell_c + \ell_j}{\Delta T_s}$$

where ΔT_s is the time between stress waves. Re-writing gives:

$$\ell_j = \left(\frac{da}{dt}\right)_T \cdot \Delta t_s - \ell_c$$

From the fractographs it is possible to estimate the percentage of dimpled mechanical rupture relative to the flat corrosion rupture, and thus to obtain an expression for ℓ_c in terms of ℓ_j. So that

$$\ell_c = (\text{constant})\ \ell_j$$

Since $\left(\frac{da}{dt}\right)_T$ is known by measuring the amount of slow crack growth in a given length of time, and Δt_s can be estimated from the SWE recordings, it is possible to calculate a value of ℓ_j.

It must be noted that the value of ℓ_j obtained in this way is the apparent amount of forward crack growth by a single discontinuous jump. The forward crack growth per unit thickness, $\ell_j(\text{For.Adv/Th.}) = (\ell_j)$ x (the number of grains involved in dimpled rupture per thickness). In this case the number of grains involved per unit thickness is just the number of grains across the thickness (60), times the number of active crack paths (1), times the percentage of the fracture surface that is dimpled. Therefore

$$\ell_j(\text{For.Adv./Th}) = (\ell_j)(60)(1)(\%\ \text{dimpled rupture}).$$

Table III lists the values of ℓ_j(For.Adv./Th) obtained in this way as a function of the stress intensity factor.

Since Fig. 6 shows that the crack growth rate is proportional to K^2, the number of grains failing by dimpled rupture as the crack advances may be proportional to the crack-tip displacement so that

$$\ell_j(\text{For.Adv./Th}) \propto \frac{K^2}{2\sigma_{ys}E}$$

Crack tip displacement values are given in Table III as a function of the stress intensity. The calculated values of ℓ_j are about an order of magnitude smaller than the corresponding crack tip displacement.

VI. DISCUSSION

A. General

This investigation has shown that two distinct mechanisms are involved in stress corrosion cracking, a mechanical process dependent on the stress intensity and an electrochemical, thermally activated process. The relative amounts of each are dependent on both the stress intensity level and the environmental temperature.

The crack propagation rate is strongly dependent on the environmental temperature. However, the dependence of the crack propagation rate on the stress intensity level is independent of temperature. These features are elaborated on in the following section.

B. Mechanical and electrochemical aspects

The calculated value of the width of a crack jump is based on a semi-empirical expression derived from experimental work by Gerberich[9] for much larger stress waves, and thus only provides an order of magnitude estimate of the width, Δw, of the crack jump. Table III shows that the calculated value of Δw is on the order

of 1 grain width. Similarly, the value of ℓ_j is dependent on the number of stress waves per second and the possibility that many low energy waves were not detected makes only an order of magnitude estimate possible.

The average value of the apparent activation energy based on the curves in Fig. 10 is 11,200 cal/mole. Values reported[10] for the activation energy range from 12,000 to 14,000 cal/mole.

The electrochemical component of SCC has been thoroughly investigated. It describes the propagation of stress corrosion cracks in the metal-enviroment system as resulting from localized anodic dissolution of the plastically deforming solid solution within the precipitate free zone along the grain boundary.

Two models have been proposed to explain the stress corrosion phenomenon. An electrochemical process described above has been widely proposed and recently supported by Sedricks, Green and Novak[15] for Al-Zn-Mg alloy in an aqueous chloride solution. Jacobs[16] has proposed a new model similar to an early model by Dix[17,18] which requires corrosion along a continuous anodic path combined with mechanical tearing of the metal at the tip of a corrosion crevice. In Jacob's model the anodic path is continuous, but instead of consisting of a single phase it consists of two phases ($MgZn_2$ and the Al matrix) which alternate as electrodes. Crack propagation occurs by a cyclic repetition of corrosion of the anodic $MgZn_2$ particles and mechanical fracture between particles. The results of this investigation support Jacob's theory -- a two step growth process as evidenced by stress wave emission and fractographic results.

VII. CONCLUSIONS

1. The crack growth rate for the SCC process was strongly dependent on temperature with an apparent activation energy of 11.2 kcal/mole. The crack growth rate was also proportional to K^2.
2. SWE techniques showed that discontinuous cracking was occurring. It also provided an estimate of the time between discontinuous jumps.
3. The frequency and amplitude of stress waves increased with increasing stress intensity for any given temperature.
4. Both mechanical and electrochemical fracture in the SCC region was found to be intergranular and the amount of dimpled rupture to be proportional to the square of the stress intensity.
5. Using SWE results and fractographic evidence, order of magnitude estimates of the length and width of the discontinuous jumps were possible. The width was estimated to be on the order of 1 grain, while the forward advance per unit thickness of the crack due to one discontinuous jump was estimated to be about 1 micron.
6. The stress corrosion cracking mechanism is concluded to be a two step process combining an electrochemical and mechanical process.

ACKNOWLEDGMENTS

The author wishes to express his appreciation to Professors Earl Parker and Victor F. Zackay and especially to Mr. William Gerberich for their advice and support. Many thanks are also due to the staff of the Inorganic Materials Research Division of the Lawrence Radiation Laboratory, in particular to John Holtius (fabrication), Phila Witherell and Mamie Brown (Photography), Gloria Pelatowski (preparation of line drawings), George Georgakopoulos (Scanning Electron Microscopy), and to the Graphic Arts Department. Thanks are also due to Carol Keenon (preparation of manuscript).

This work was done under the auspices of the U. S. Atomic Energy Commission through the Inorganic Materials Research Division of the Lawrence Radiation Laboratory.

REFERENCES

1. Metals Handbook, American Society for Metals, Vol. 1, 8th ed., p. 917.

2. Aluminum, American Society for Metals, Vol. 1, 1967, p. 13.

3. W. Gruhl, The Temperature Dependence of the SCC of $AlZnMg_3$, Z. Metallkunde 53, 670 (1962).

4. ASTM Standards, American Society for Testing and Materials, 1969, p. 206.

5. W. F. Brown and J. E. Srawley, Plain Strain Crack Toughness of High Strength Metallic Materials, ASTM-STP410, 1966.

6. W. W. Gerberich and C. E. Hartbower, Some Observations on Stress Wave Emission as a Measure of Crack Growth, Int. J. of Fracture Mechanics 3 (3), 185 (1967).

7. C. E. Hartbower, W. W. Gerberich, and P. P. Crimmins, Monitoring Subcritical Crack Growth by Detection of Elastic Stress Waves, Welding J. Research Supplement, January 1968.

8. C. E. Hartbower, W. W. Gerberich, and H. Liebowitz, Investigations of Crack Growth Stress-Wave Relationships, Eng. Fracture Mechanics 1, 291 (1968).

9. W. W. Gerberich, V. F. Zackay, E. R. Parker, and D. Porter, The Role of Grain Boundaries on Crack Growth, 16th Sagamore Army Materials Research Conference, August 19-22, 1969.

10. D. Tromans and R. S. Pathania, The Importance of Hydrogen in SCC of Aluminum Alloys, The Electrochemical Society, Extended Abstracts, Oct. 1969.

11. D. O. Sprouls and R. H. Brown, Stress Corrosion Mechanisms for Aluminum Alloys, Proceedings of Conference on Fundamental Aspects of SCC,(Ohio State University, 1967) p. 466.

12. A. F. Beck and P. R. Sperry, The Relationship Between Structure and Susceptibility to Stress Corrosion in Aluminum-Magnesium Alloys, Ibid, p. 513.

13. M. O. Spiedel, Interactions of Dislocations with Precipitates in High Strength Aluminum Alloys and Susceptibility to SCC, Ibid, p. 561.

14. F. H. Haynie and W. K. Boyd, An Electrochemical Study of the Mechanisms of SCC in an Al-Zn-Mg Alloy, Ibid, p. 580.

15. A. J. Sedricks, J. A. S. Green, and D. L. Novak, Comparison of Corrosion and Stress Corrosion Behavior of a Ternary Al-Zn-Mg Alloy, Met. Trans. Vol. 1, July 1967.

16. A. J. Jacobs, The Mechanisms of Stress Corrosion Cracking in 7075 Aluminum, Proceedings of Conference on Fundamental Aspects of SCC, (Ohio State University, 1967) p. 530.

17. R. B. Mears, R. H. Brown, and E. H. Dix, Jr., Symposium on Stress Corrosion Cracking of Metals, ASTM-AIME, Philadelphia, 1944, p. 723.

18. E. H. Dix, Jr., Acceleration of the Rate of Corrosion by High Constant Stresses, AIME Trans. 137, 11 (1940).

Table I. Fracture analysis data for determining stress intensity and crack growth rates of 7075-T6 Al

T (°C)	a_i (in.)	a_f (in.)	P_i (lbs.)	P_f (lbs.)	K_i (psi-in.$^{1/2}$)	K_f (psi-in.$^{1/2}$)	K_{ave} (psi-in.$^{1/2}$)	Δt (min)	Δa (in.)	da/dt (in./min)
10	0.737	0.785	1464	1460	36090	39470	37780	47.0	0.048	0.0010
23	0.735	0.805	1850	1805	45430	50730	48080	14.8	0.070	0.0047
23	0.735	0.805	1820	1780	44700	50030	47360	5.2	0.070	0.0135
23	0.750	1.155	1210	898	30580	52830	41700	67.8	0.405	0.0060
23	0.750	0.815	1540	1497	38920	39910	39410	13.0	0.065	0.0050
23	0.745	0.815	1385	1342	34670	38460	36560	19.3	0.070	0.0036
23	0.702	0.745	1584	1540	36540	38550	37540	21.4	0.043	0.0020
23	0.705	0.760	1475	1430	32210	36840	35530	14.7	0.055	0.0037
23	0.725	0.995	1145	968	27590	40040	33810	73.0	0.270	0.0037
23	0.725	0.725	1400	1400	33730	33730	33730	46.3	--	--
23	0.705	0.770	1365	1320	31660	34660	33160	25.5	0.065	0.0026
23	0.745	0.825	1160	1110	29040	32440	30740	26.7	0.080	0.0030
23	0.740	0.835	968	923	24000	27510	25760	26.0	0.090	0.0035
23	0.753	0.830	935	891	23760	26300	25030	47.0	0.077	0.0016
23	0.715	0.825	924	880	21840	25720	23780	60.0	0.110	0.0018
23	0.710	0.905	634	598	14850	20510	17680	230.0	0.195	0.00085
23	0.900	0.970	433	414	1555	18850	17200	204.0	0.070	0.00034
23	0.900	0.900	260	260	9250	9250	9250	328.0	--	--
32	0.670	0.715	2160	2110	46900	49880	48400	5.2	0.045	0.0086
33	0.720	0.745	1470	1420	35080	35540	35310	6.7	0.025	0.0037

Table I. (continued)

T (°C)	a_i (in.)	a_f (in.)	P_i (lbs)	P_f (lbs)	K_i (psi-in.$^{1/2}$)	K_f (psi-in.$^{1/2}$)	K_{ave} (psi-in.$^{1/2}$)	Δt (min)	Δa (in.)	da/dt (in./min)
33	0.760	0.800	924	880	23800	24490	24150	7.6	0.040	0.0052
43	0.712	0.775	1462	1420	34370	37650	36010	4.2	0.063	0.0150
43	0.745	0.805	1022	979	25580	27510	26550	9.4	0.050	0.0053
43	0.690	0.735	1120	1080	25250	26520	25890	5.3	0.045	0.0085
48	0.715	0.770	2019	1960	47730	51470	49600	1.4	0.055	0.0402
53	0.685	0.755	1558	1520	34800	38780	36790	2.8	0.070	0.0250
53	0.700	0.790	1085	1046	24930	28550	26740	7.5	0.090	0.0120
53	0.690	0.770	1092	1045	24620	27440	26030	11.4	0.080	0.0070
60	0.745	0.760	1270	1200	31790	30910	31350	0.6	0.015	0.0268
62	0.800	0.810	940	890	26160	25260	25710	0.8	0.010	0.0122
62	0.735	0.760	1030	980	25300	25250	25270	1.2	0.025	0.0220
68	0.669	0.745	2185	2115	47350	48710	48030	1.1	0.076	0.0724
73	0.745	0.790	1440	1366	36050	37280	36660	0.9	0.045	0.0500
73	0.695	0.715	1121	1080	25520	25580	25550	1.0	0.020	0.0200
73	0.725	0.745	1022	972	24620	24330	24480	0.75	0.020	0.0267

Table II. Mechanical properties of 7075-T6 aluminum

	Y.S. (0.2% offset) (psi)	T.S. (psi)	% Elong. (1.0 in. gage)	% Reduction of area	Hardness R_b
As received material	70,400	81,000	10	35	90.5
	71,500	80,300	12	28	90.5
	71,500	81,000	12	20	91.0
	72,600	81,000	12	32	90.5
	71,500	80,300	12	24	90.0
Average values	71,500	80,700	11.6	28	90.5
Rolled, solution H.T., and aged	56,600	79,400	14.6	27	84.0
	56,500	77,800	17.0	28	84.5
	56,500	78,700	14.2	23	84.5
	56,500	79,300	14.3	26	84.0
	58,000	80,000	15.9	26	85.0
Average values	56,800	79,040	15.2	26	84.0

Commercial specifications Y.S. (0.2% offset) = 73,000, T.S. = 83,000, % Elong. (2 in. g) = 11

Table III. SWE Analysis of data from SCC tests

K_{ave} (psi-in.$^{1/2}$)	T (°C)	No. SWE/SEC	Δt_s (sec)	% Dimpled rupture	da/dt (in./sec$\times 10^5$)	ℓ_j(forward/adv/Th (in.)$\times 10^4$)
25,400	23	1.6	0.625	20	2.7	0.375
36,200	33	4.0	0.25	33	6.2	0.563
48,300	23	20.0	0.05	80	7.8	1.5

K_{ave}	SWE amplitude (in.)	g (ft/sec$^2\times 10^4$)	ΔA (in.$^2\times 10^6$)	ΔW (in.$\times 10^3$)	$K^2/2\sigma_{YS}E$ (in. $\times 10^3$)
25,400	1.07	2.3	0.24	0.64	0.52
36,200	1.7	3.6	0.18	3.2	1.1
48,300	2.7	5.7	0.16	0.94	1.8

FIGURE CAPTIONS

NOTE: In all fracture surface photomicrographs the direction of crack growth is vertical from the bottom to the top of the page.

Fig. 1 Schematic of the SEN specimen geometry

Fig. 2 Schematic of the tensile specimen geometry

Fig. 3 Schematic of the test setup

Fig. 4 Instron loading setup showing placement of the tubing around the SEN specimen

Fig. 5 Actual instrument setup for monitoring and recording SWE

Fig. 6 Crack growth rate as a function of stress intensity for constant temperature (23°C)

Fig. 7 Crack growth rate as a function of temperature for $K_{Avg} = 48.3 \times 10^3$ psi-in$^{1/2}$

Fig. 8 Crack growth rate as a function of temperature for $K_{Avg} = 36.2 \times 10^3$ psi-in$^{1/2}$

Fig. 9 Crack growth rate as a function of temperature for $K_{Avg} = 25.4 \times 10^3$ psi-in$^{1/2}$

Fig. 10 Superimposed curves of Figs. 7, 8, and 9

Fig. 11 (A) The actual SEN specimen

(B) Side view showing the direction of crack propagation across the SEN specimen

Fig. 12 (A) Edge veiw in the longitudinal direction of the as received material

(B) Top view of the as received material

(C) Edge view in the longitudinal direction of the material in the cold worked and heat treated condition

(D) Top view of the material in the same condition

Fig. 13 Macroscopic fracture appearance of the test specimen, region (a - b) is the pre-fatigue cracked area

(b - c) the slow crack growth region

(c - d) unstable crack growth during rapid loading to failure after the slow crack growth had been recorded

(A) K_{Avg} = 37540 psi-in$^{1/2}$, T = 23°C

(B) K_{Avg} = 27780 psi-in$^{1/2}$, T = 23°C

(C) K_{Avg} = 36790 psi-in$^{1/2}$, T = 23°C

(D) K_{Avg} = 36560 psi-in$^{1/2}$, T = 23°C

Fig. 14 Edge view of the fracture path of specimens

(A) K_{Avg} = 48080 psi-in$^{1/2}$, T = 23°C

(B) K_{Avg} = 25030 psi-in$^{1/2}$, T = 23°C

Fig. 15 (A) Pre-fatigue crack region, not exposed to the test environment, representative of all test specimen fatigue regions

(B), (C), (D) Fracture surfaces of slow crack growth regions of a specimen tested at K_{Avg} = 36600 psi-in$^{1/2}$ and T = 73°C

Fig. 16 Fracture surface showing slow crack growth region of a specimen tested at K_{Avg} = 36600 psi-in$^{1/2}$ and T = 73°C

(A) Corrosion region

(B), (C), (D) dimpled rupture mechanical region

Fig. 17 (A) Pre-fatigue region, exposed to the test environment at 53°C, showing grain boundary cracking due to the environment

(B) Fracture surfaces of slow crack growth region of a specimen tested at K_{Avg} = 36790 psi-in$^{1/2}$ and T = 53°C

(C) Dimpled region of same specimen

(D) Predominately flat region of same specimen

Fig. 18 Same specimen as Fig. 17

(A) and (C) fracture surface of slow crack region showing textured appearance of corrosion region

(B) and (D) unstable crack growth region showing dimpled appearance

Fig. 19 Same specimen as Fig. 17, fracture surface of slow crack growth region

Fig. 20 Fracture surface of the slow crack growth region of a specimen tested at K_{Avg} = 26740 psi-in$^{1/2}$, and T = 53°C

(A) shows predominately flat corrosion appearance

(B) and (C) show flat surface appearance

(D) Small region of dimpled rupture

Fig. 21 Fracture surface of slow crack growth region of a specimen tested at K_{Avg} = 49600 psi-in$^{1/2}$, and T = 48°C, showing almost completely dimpled rupture

Fig. 22 (A) and (B) Fracture surface of slow crack growth region of a specimen tested at K_{Avg} = 36560 psi-in$^{1/2}$, and T = 23°C, showing the effect of the solution on the surface for tests run for long periods of time.

Fig. 23 Fracture surface of slow crack growth region of a specimen tested at K_{Avg} = 37780 psi-in$^{1/2}$, and T = 23°C

Fig. 24 Fracture surface of slow crack growth region of a specimen tested at K_{Avg} = 37780 psi-in$^{1/2}$, and T = 10°C

Fig. 25 Same specimen as Fig. 24

(A) and (B) Slow crack growth regions

(C) and (D) Show the effect of the environment on the pre-fatigue cracked region after 47 minutes

Fig. 26 NaCl + $AlCl_3$ test environment dried on a brass holder to compare with the actual test material. Note the completely smooth appearance.

Fig. 27 Fracture surface of a specimen, tested at K_{Avg} = 17680 psi-in$^{1/2}$ and T = 23°C, showing salt solution residue on the surface of the specimen, and the generally corroded surface appearance after 230 minutes in the test environment

Fig. 28 SWE oscillogram recordings of specimens tested at T = 23°C

(A) K_{Avg} = 25400 psi-in$^{1/2}$

(B) K_{Avg} = 36200 psi-in$^{1/2}$

(C) K_{Avg} = 48300 psi-in$^{1/2}$

Fig. 29 SWE oscillogram recordings of specimens tested at K_{Avg} = 36200 psi-$in^{1/2}$ and T = 23°C

(A) Tested in air

(B) Tested in solution

Fig. 30 SWE oscillogram recordings of specimens tested at T = 23°C

(A) An actual test where K_{Avg} = 48300 psi-$in^{1/2}$

(B) Just the equipment background noise with no load applied to the specimen

Fig. 31 SWE oscillogram recordings of specimens tested at T = 68°C

(A) An actual test where K_{Avg} = 48300 psi-$in^{1/2}$

(B) Just the equipment background noise with no load applied to the specimen

Fig. 32 SWE oscillogram recordings of specimens tested with no load applied in order to compare background noise

(A) T = 23°C

(B) T = 68°C

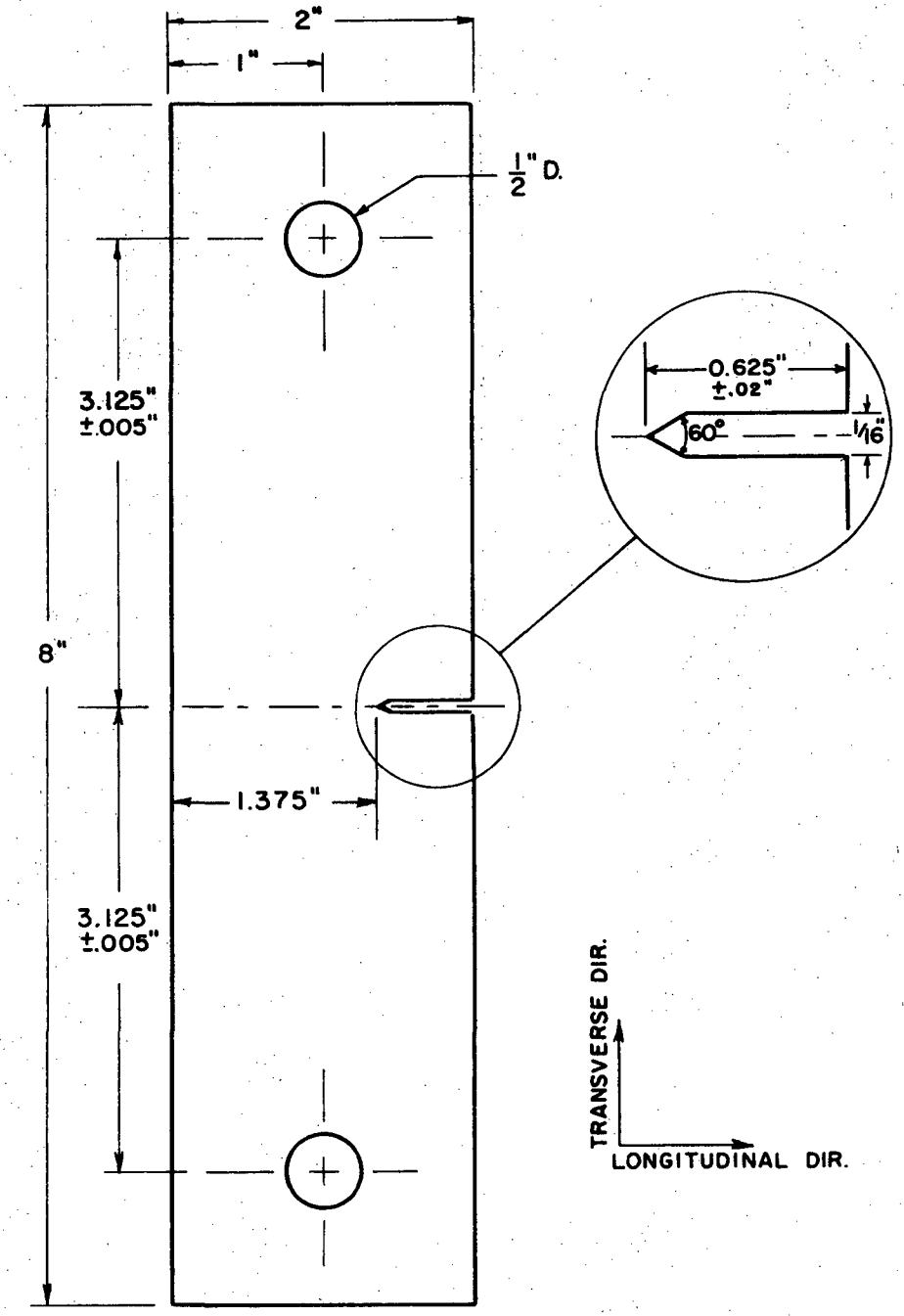

XBL 708-6423

Fig. 1

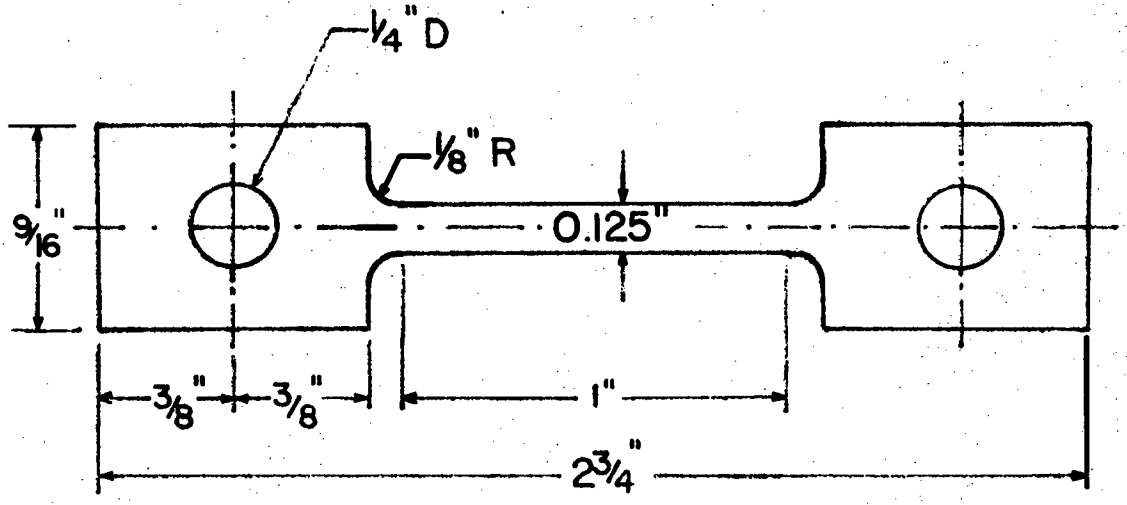

TENSILE SPECIMEN

SCALE: 2:1

XBL 698-1155

Fig. 2

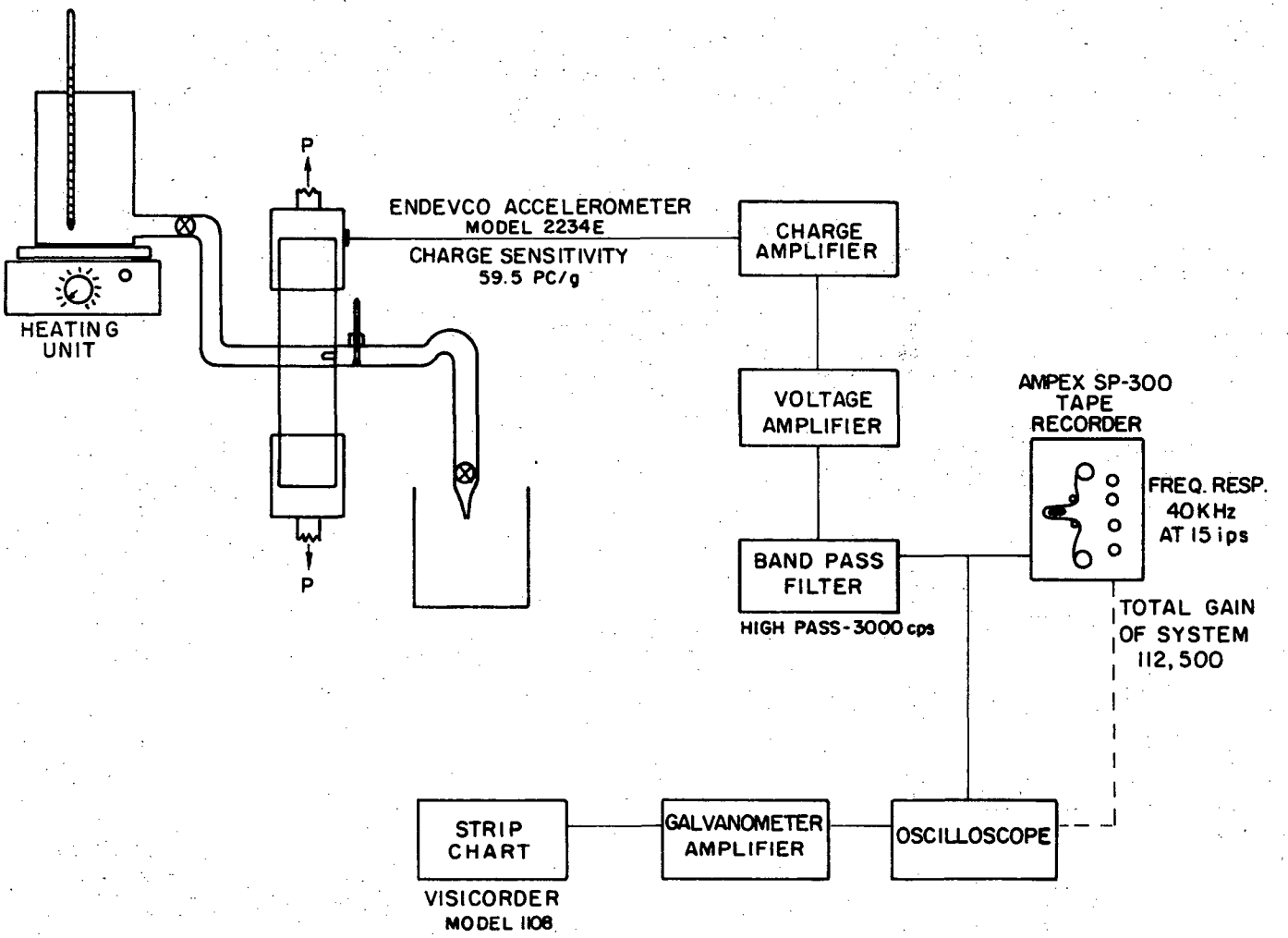
P
ENDEVCO ACCELEROMETER
MODEL 2234E
CHARGE SENSITIVITY
59.5 PC/g
CHARGE AMPLIFIER
HEATING UNIT
VOLTAGE AMPLIFIER
AMPEX SP-300 TAPE RECORDER
FREQ. RESP. 40KHz AT 15 ips
BAND PASS FILTER
HIGH PASS-3000 cps
TOTAL GAIN OF SYSTEM 112,500
STRIP CHART
VISICORDER MODEL 1108
GALVANOMETER AMPLIFIER
OSCILLOSCOPE
P
XBL 708-6421

Fig. 3

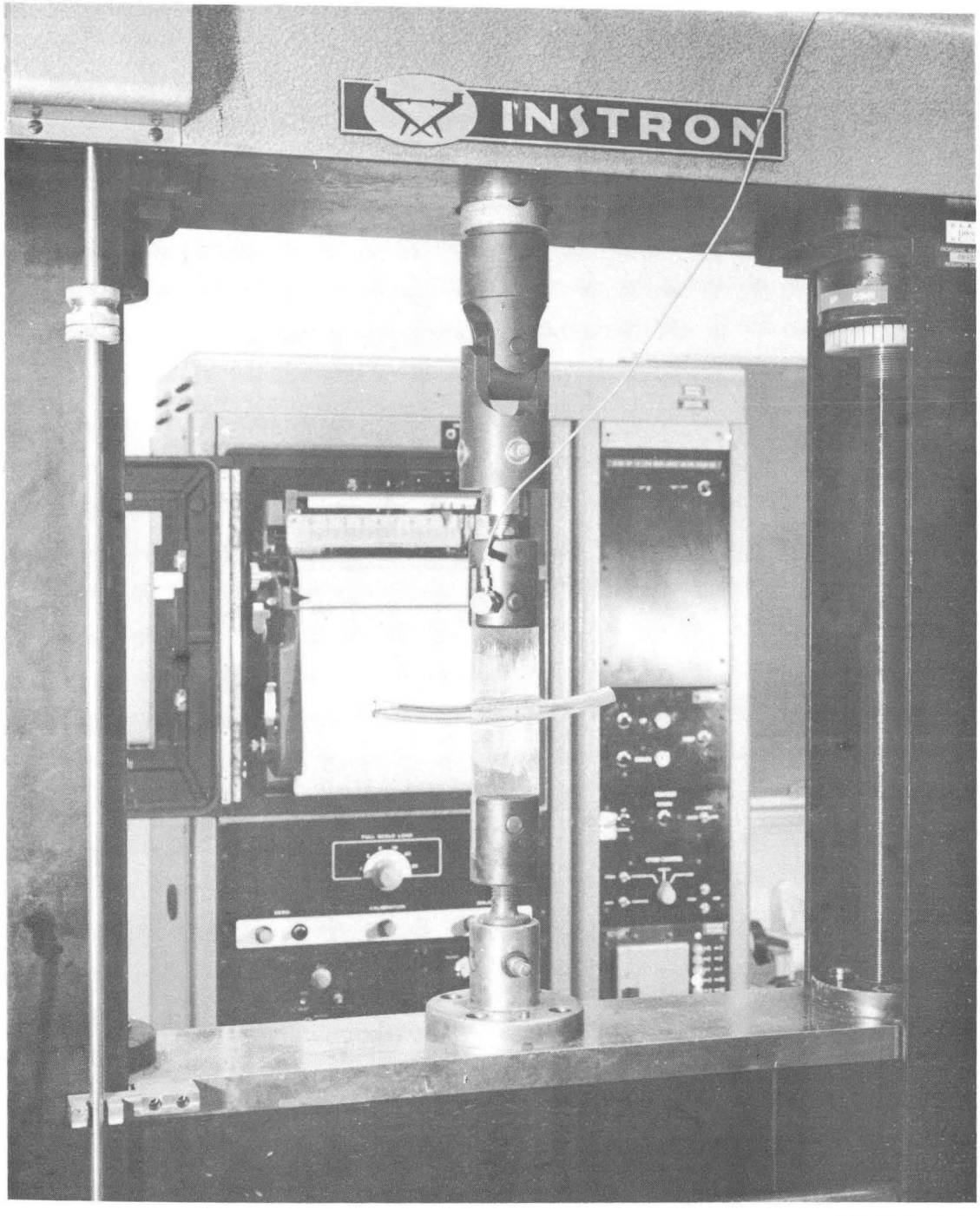

XBB707-3017

Figure 4

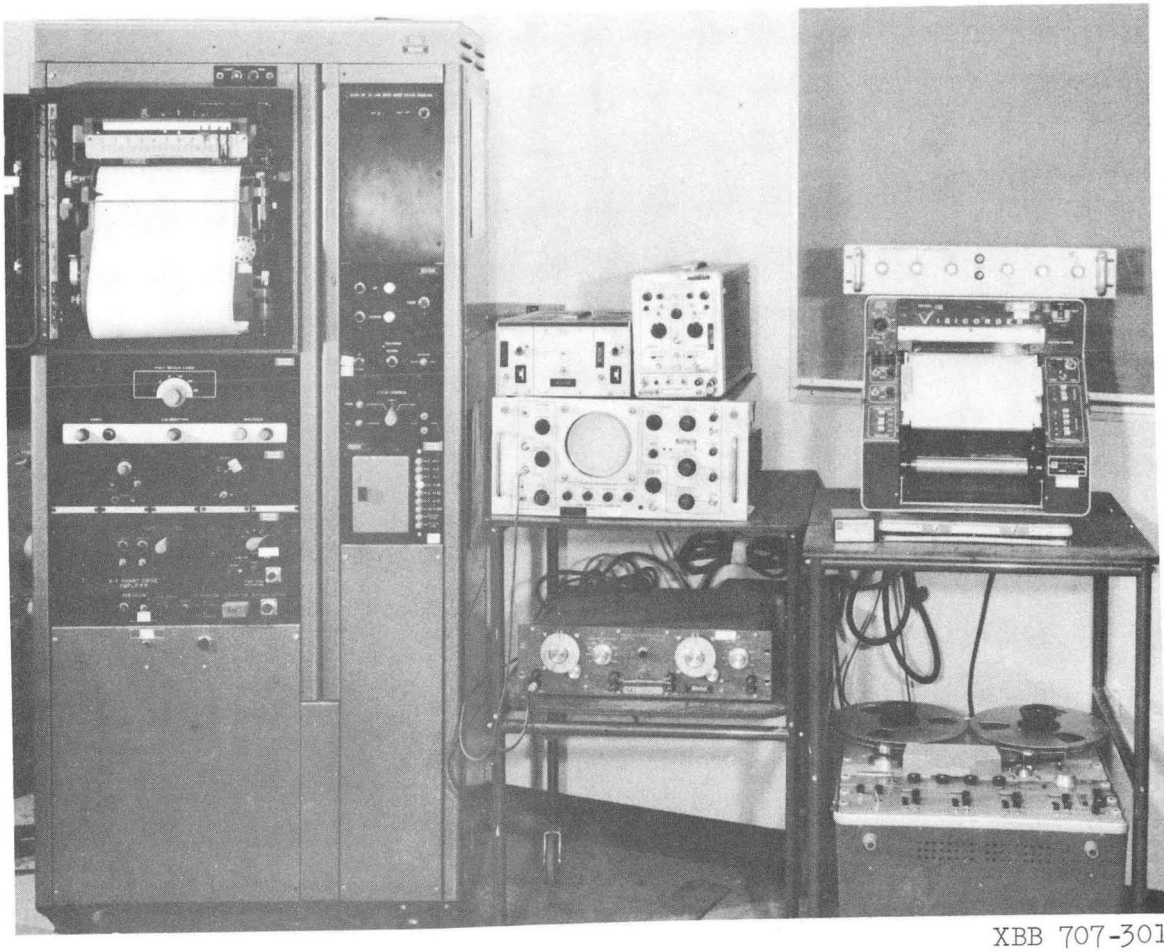

XBB 707-3019

Figure 5

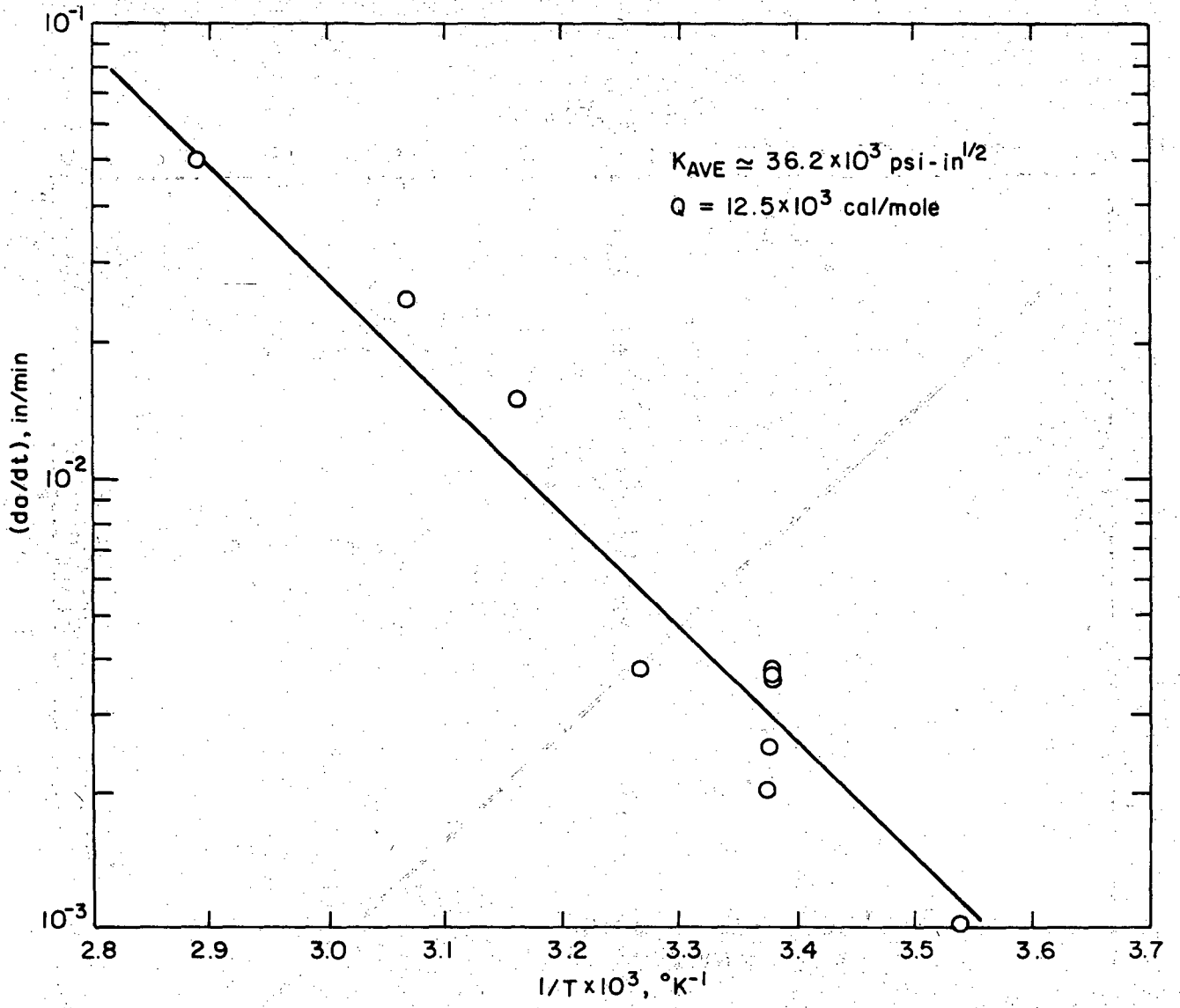

XBL 708-6419

Fig. 8

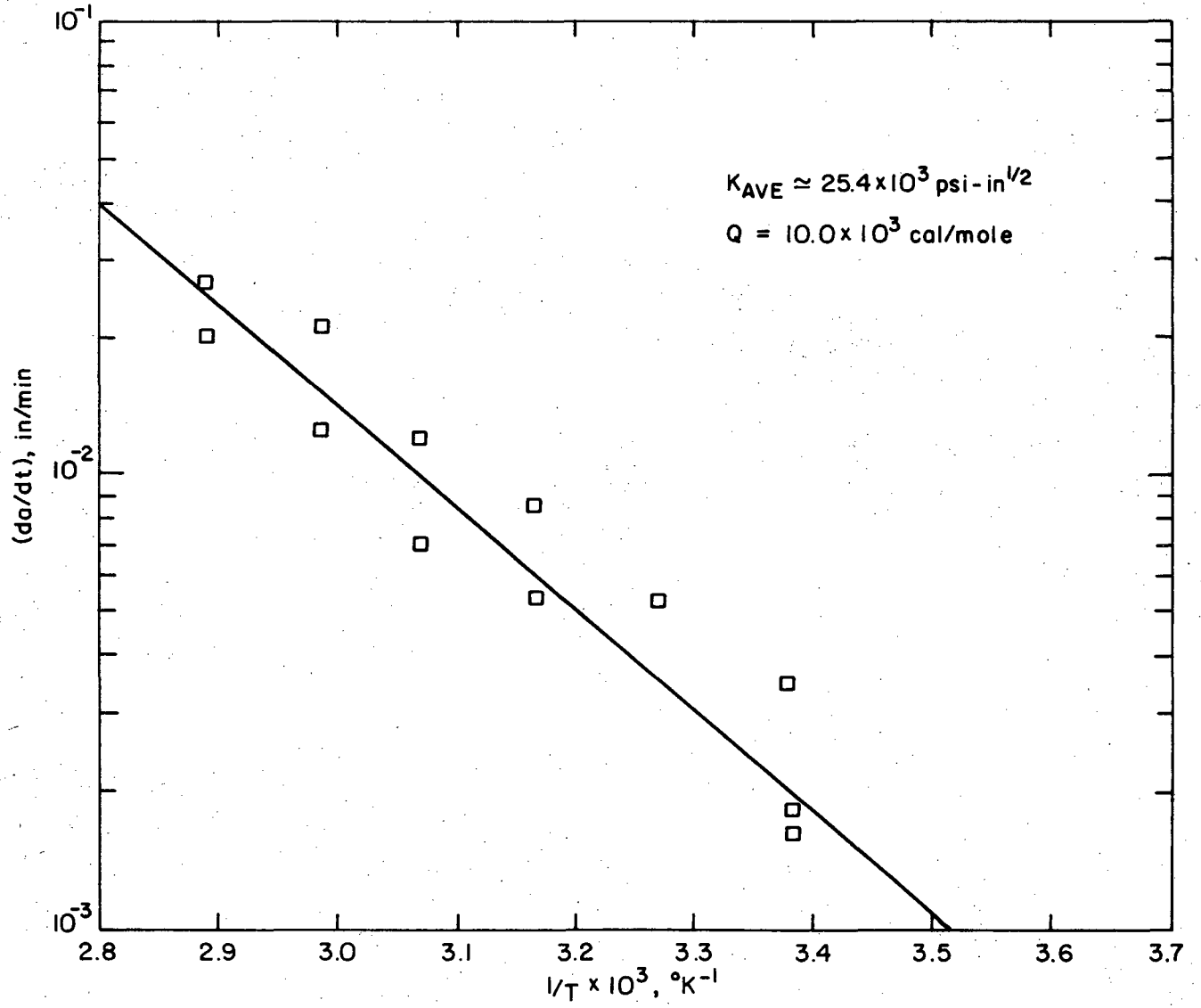

XBL 708-6418

Fig. 9

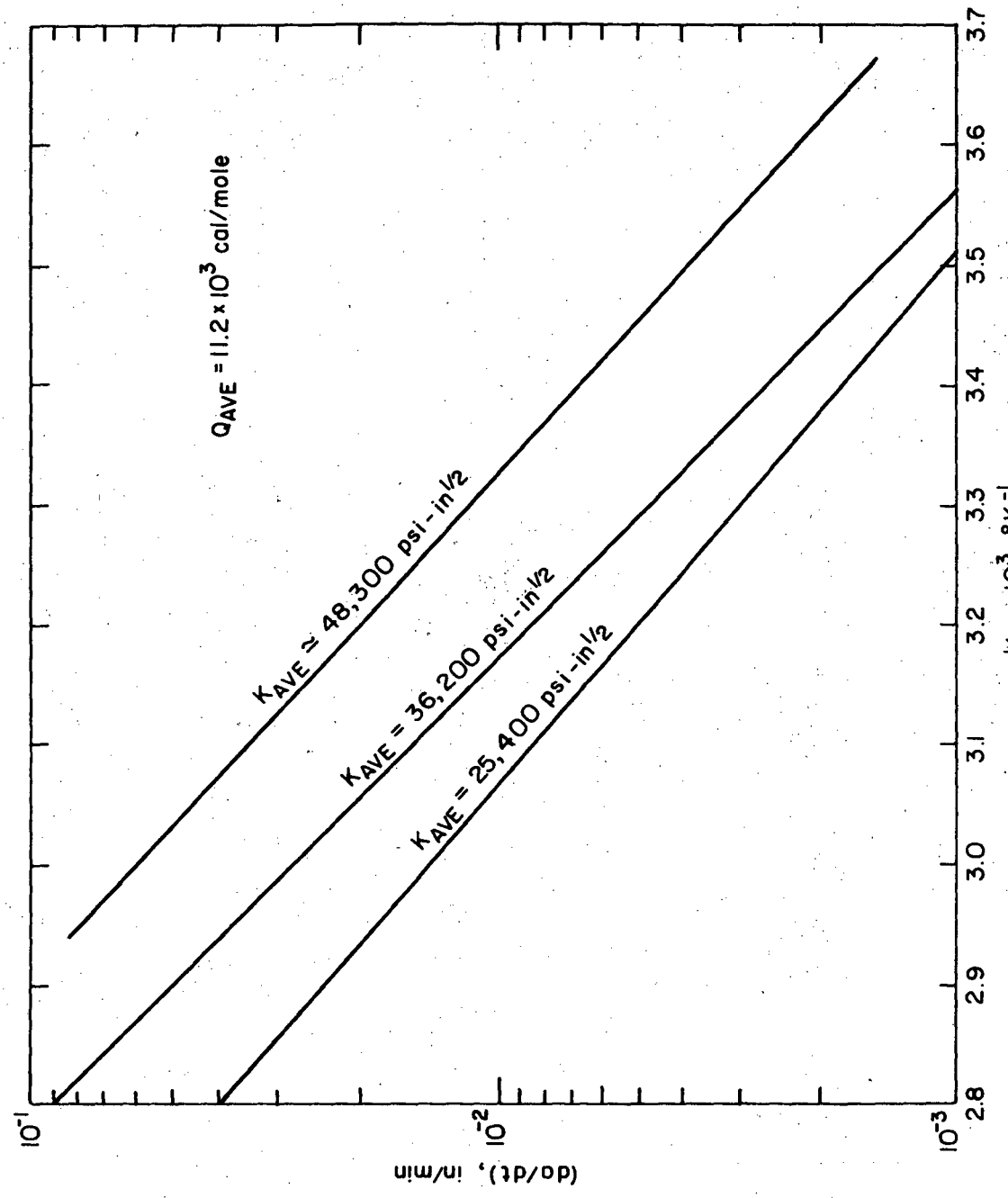

XBL 708-6417

Fig. 10

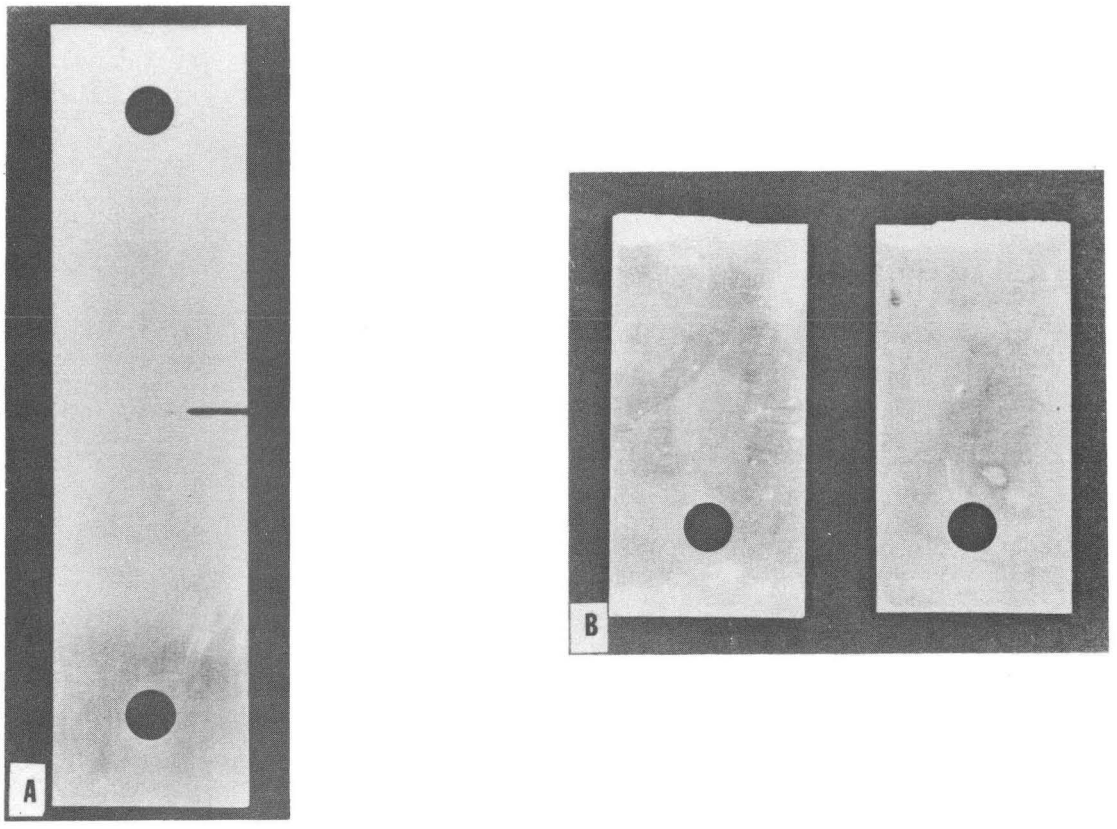

XBB 708-3809

Figure 11

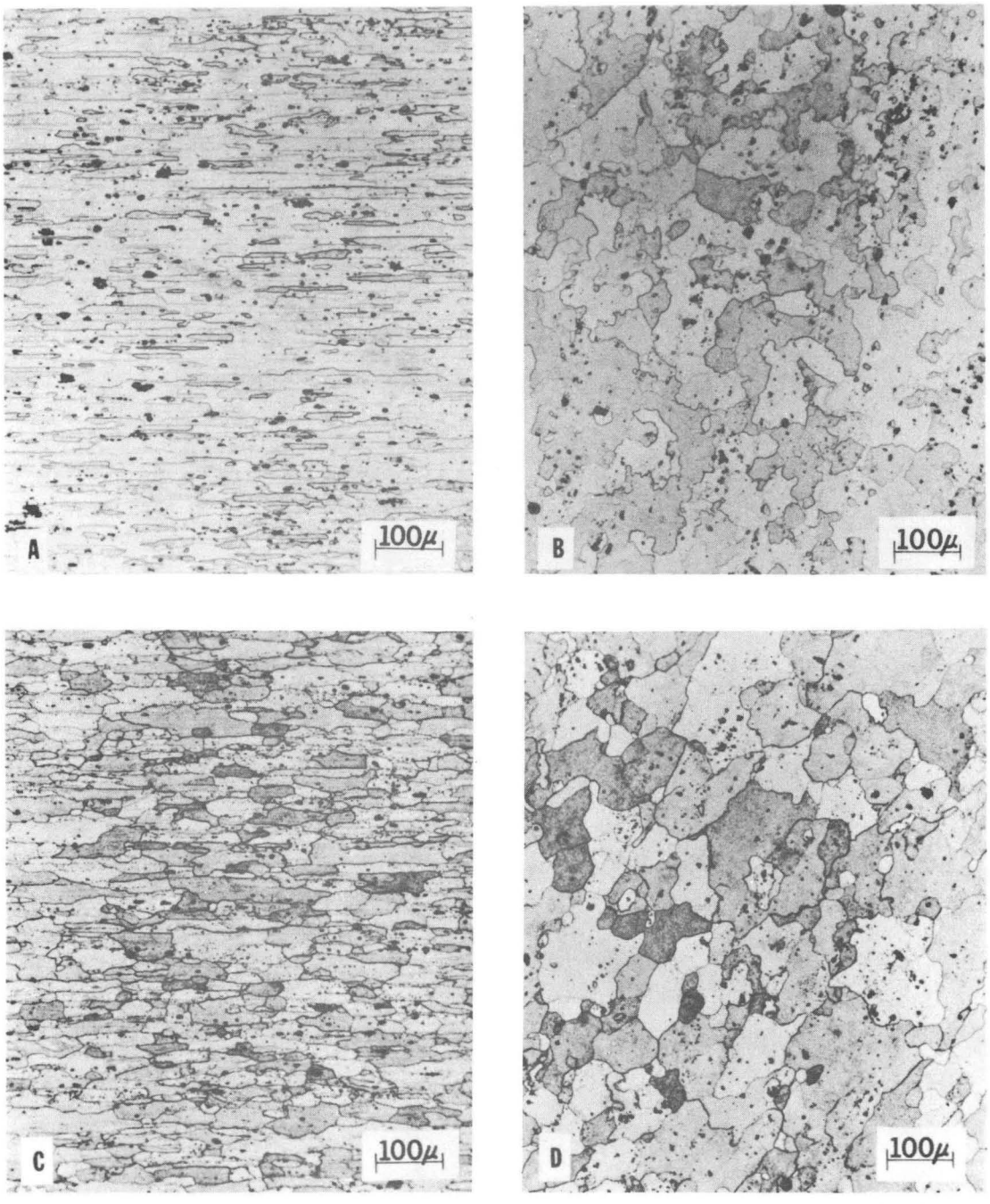

XBB 708-3810

Figure 12

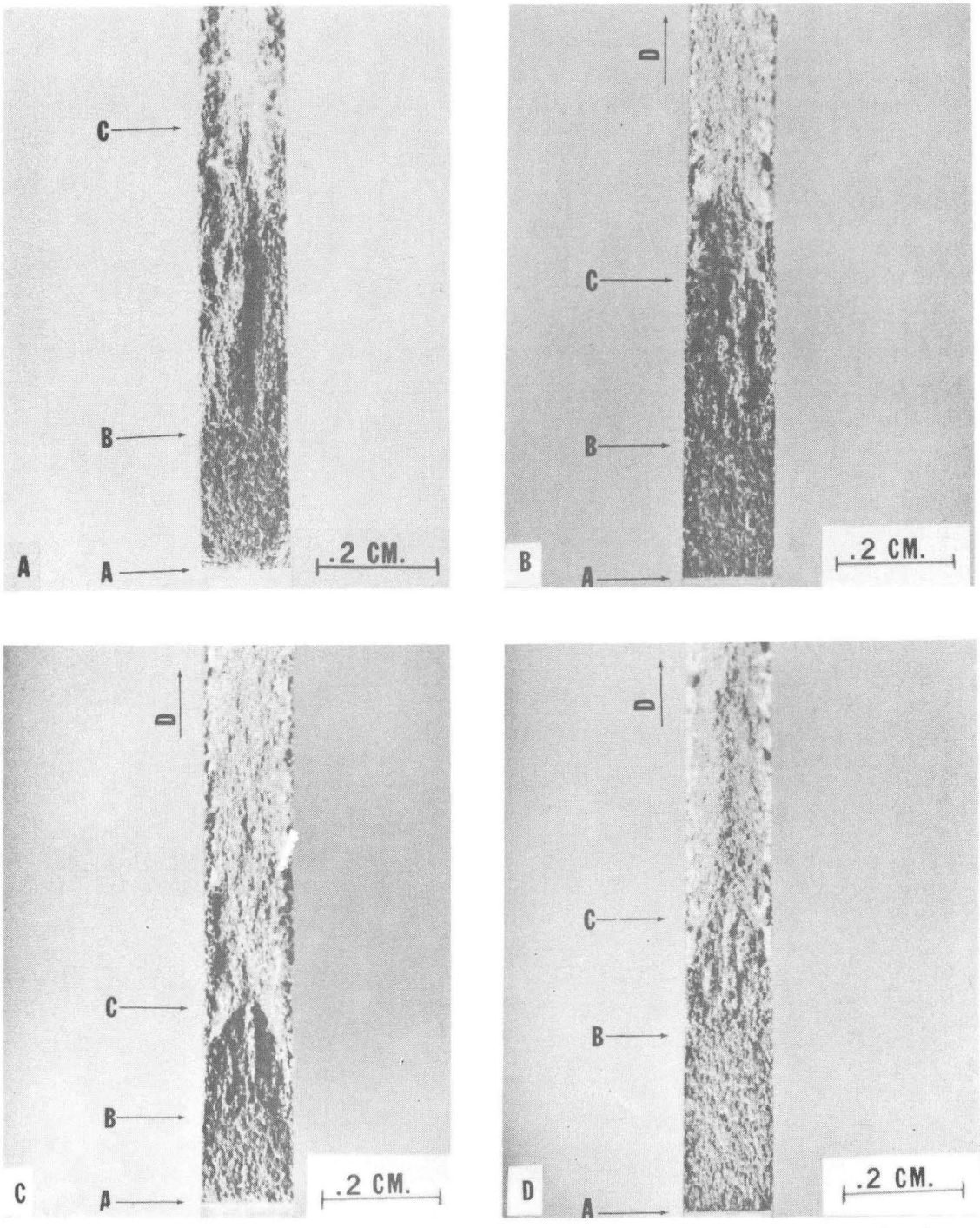

XBB708-3825

Figure 13

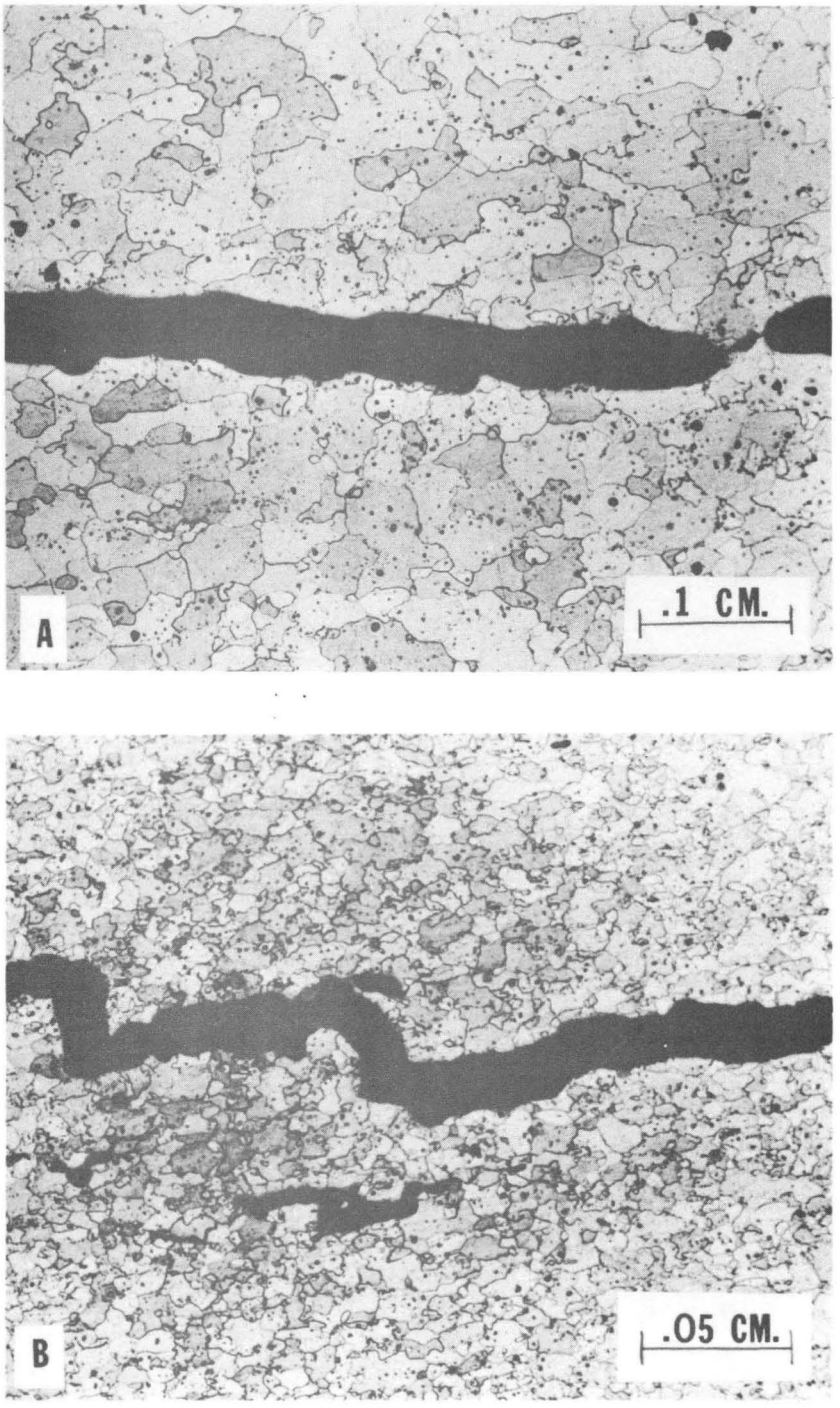

XBB 708-3811

Figure 14

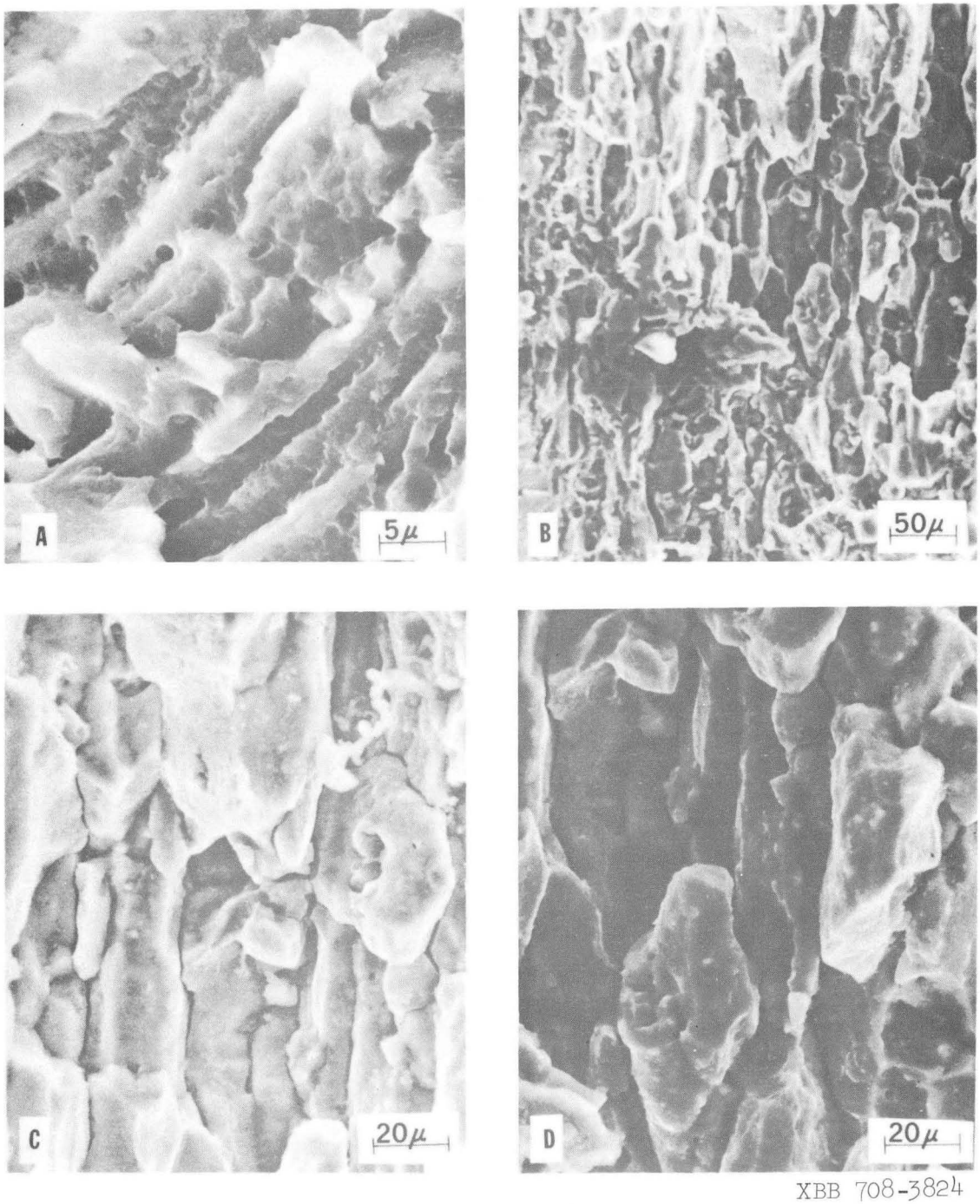

XBB 708-3824

Figure 15

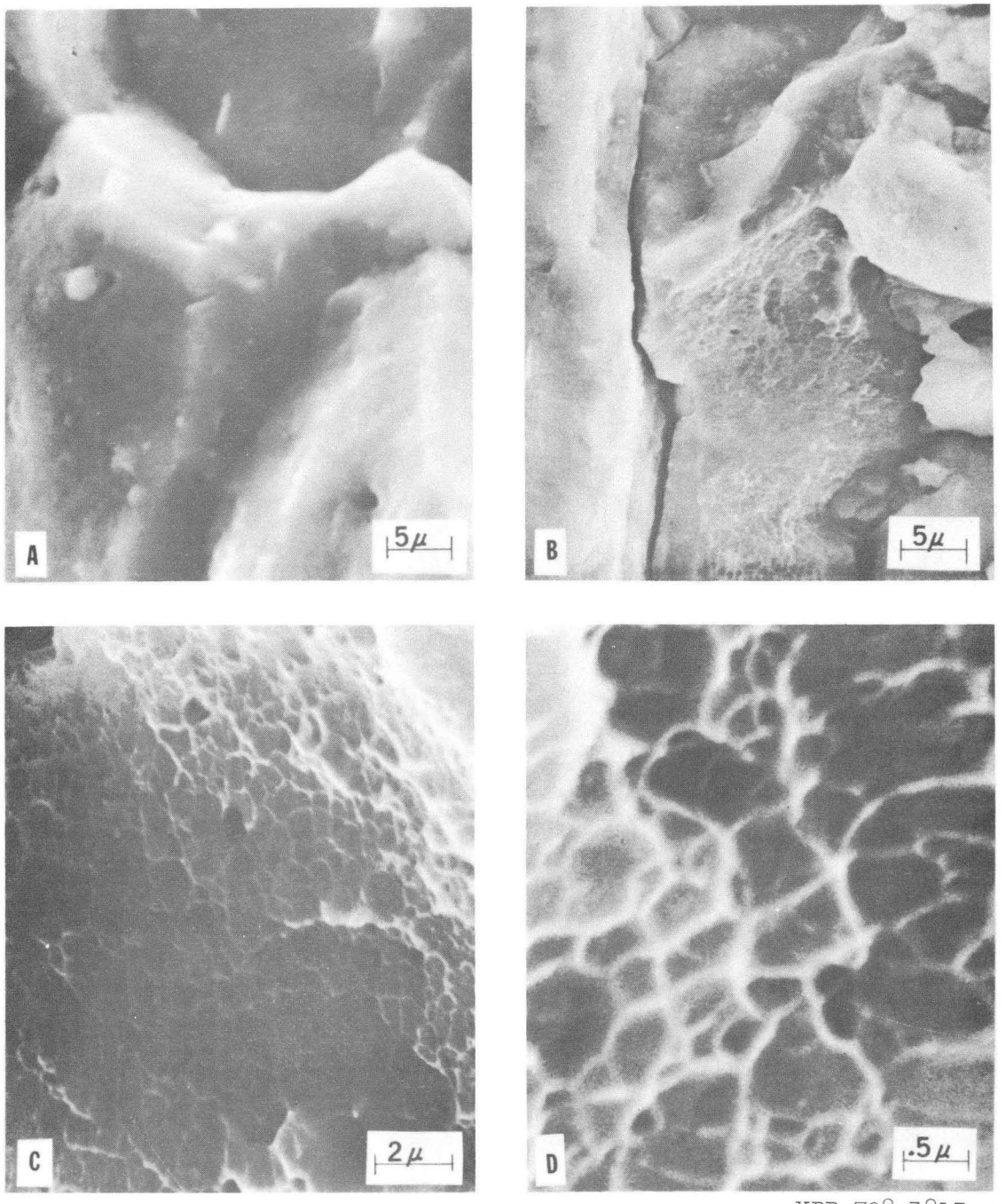

XBB 708-3815

Figure 16

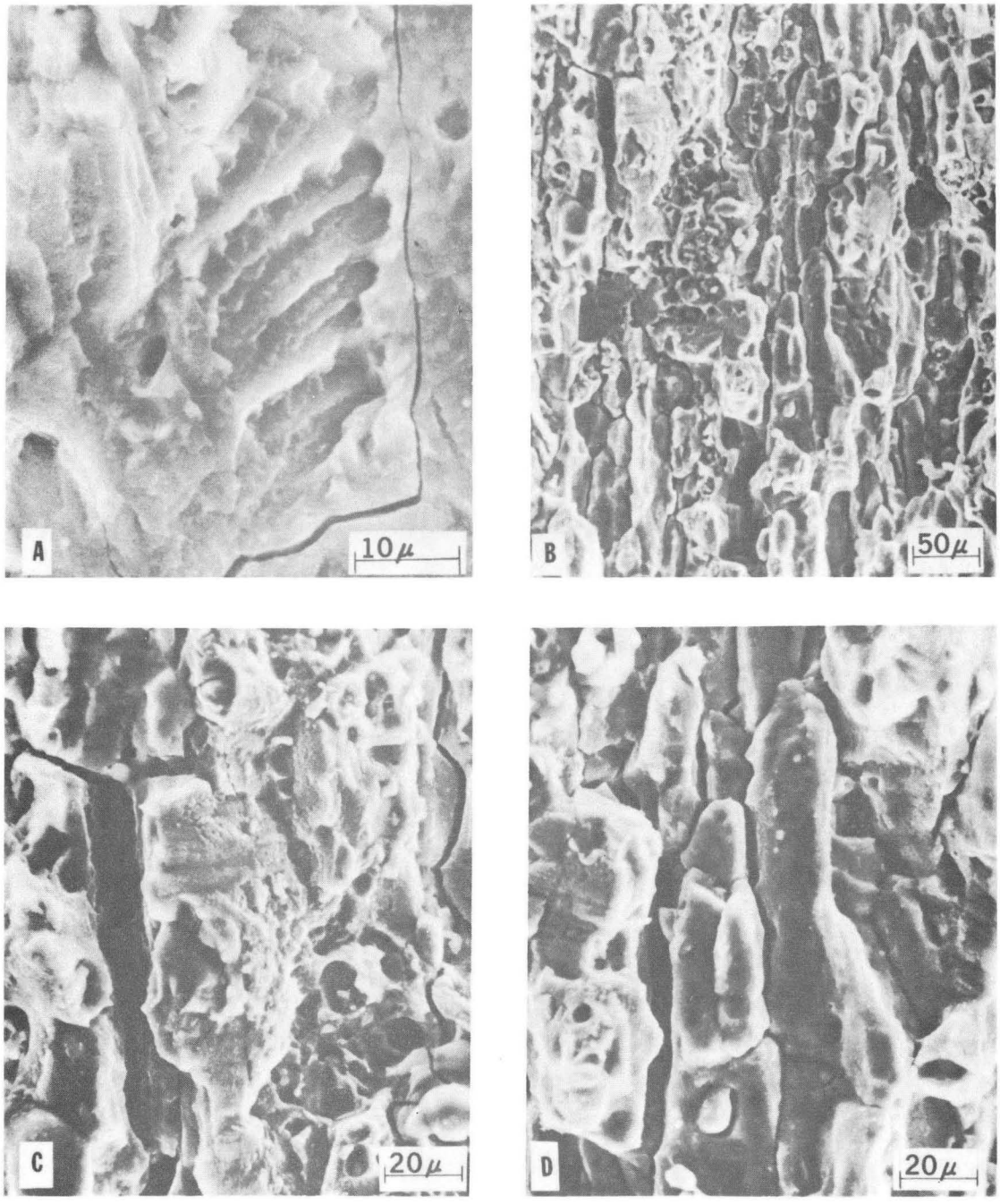

XBB 708-3817

Figure 17

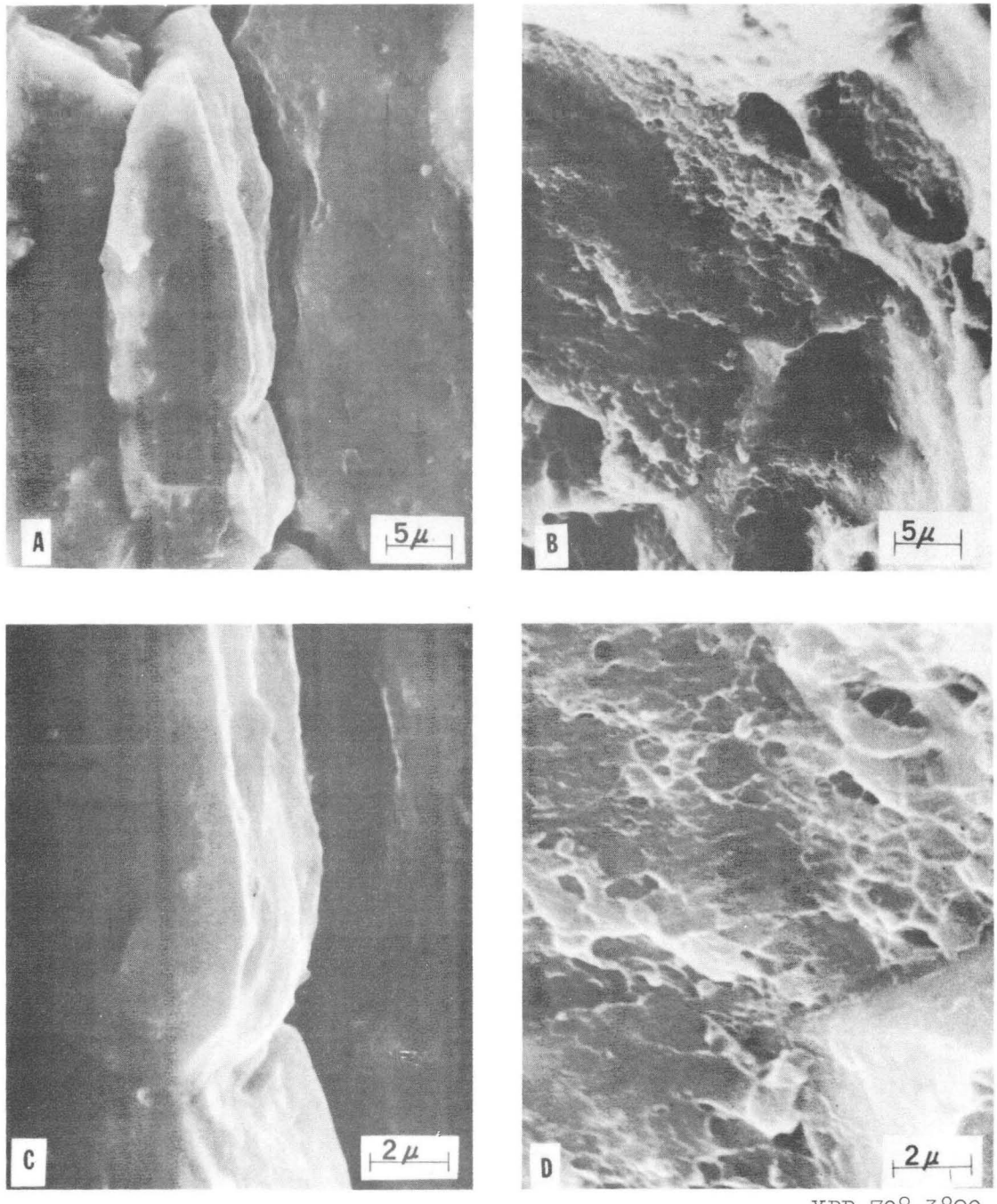

XBB 708-3820

Figure 18

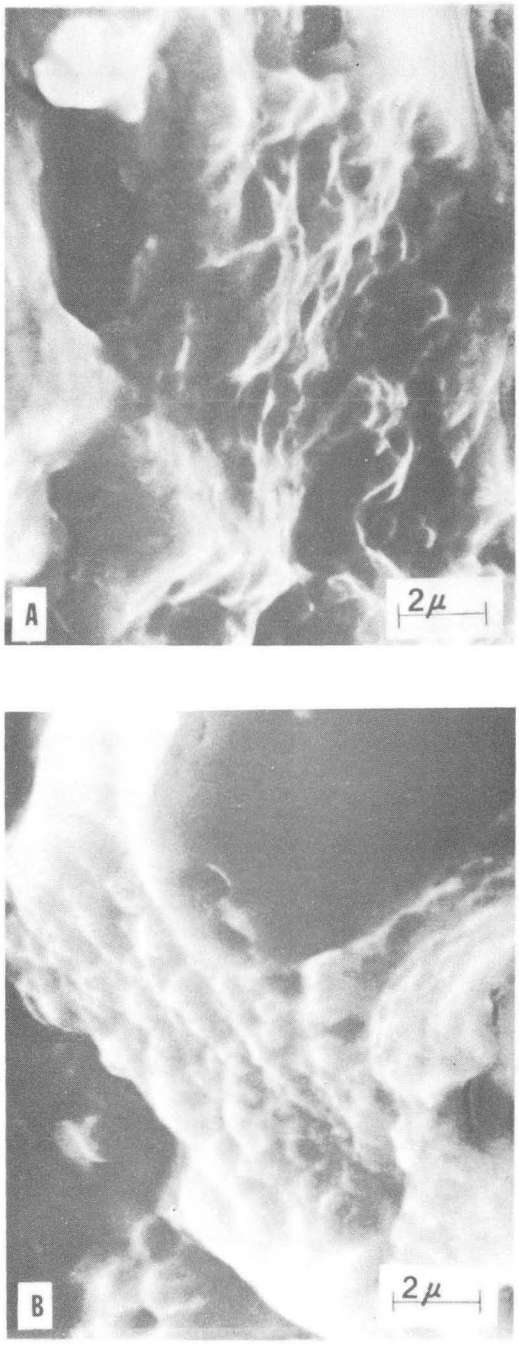

XBB 708-3822

Figure 19

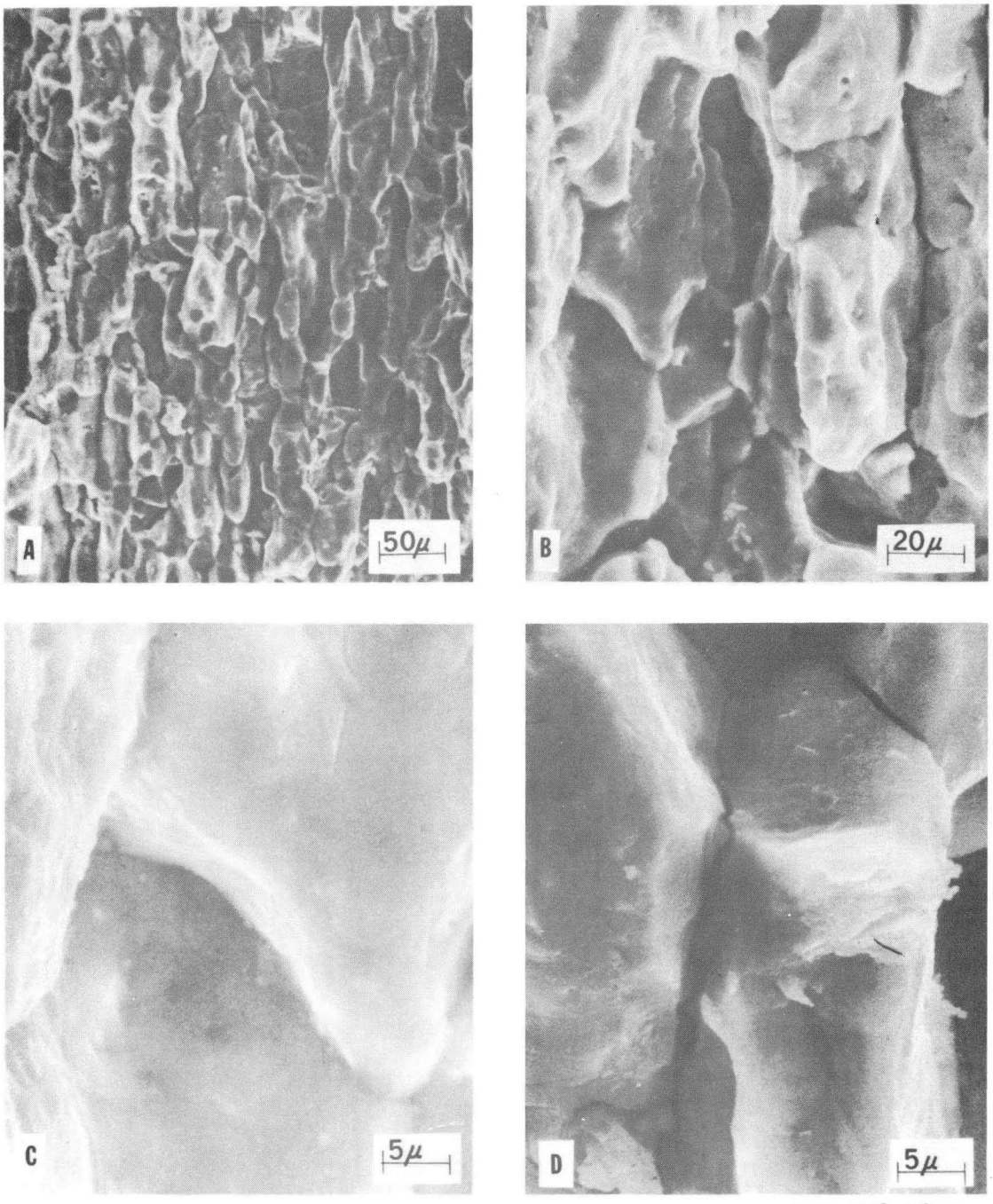

XBB 708-3813

Figure 20

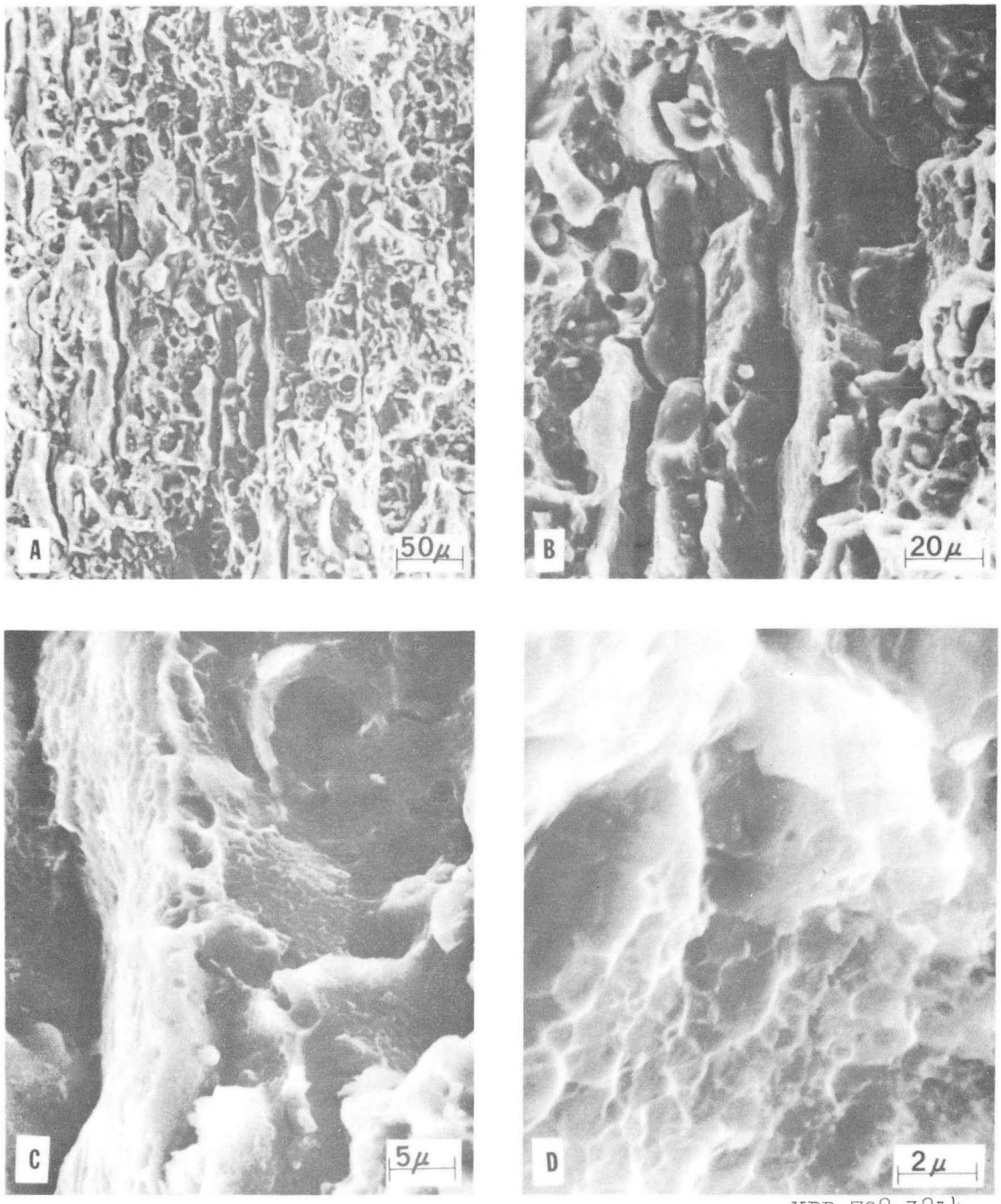

XBB 708-3814

Figure 21

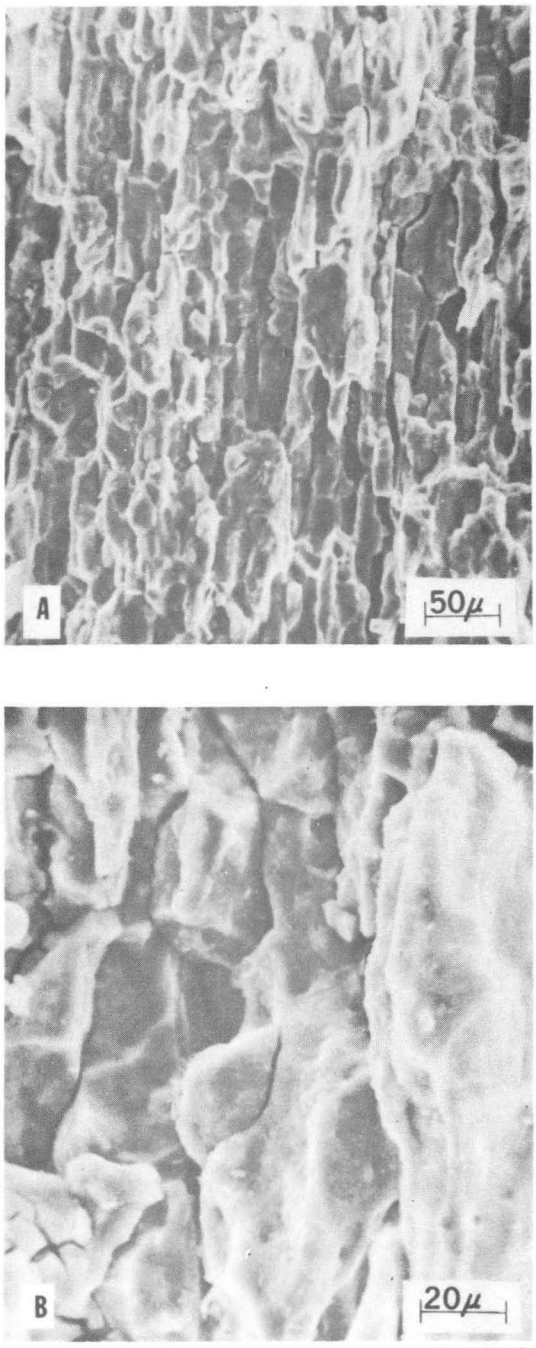

XBB 708-3818

Figure 22

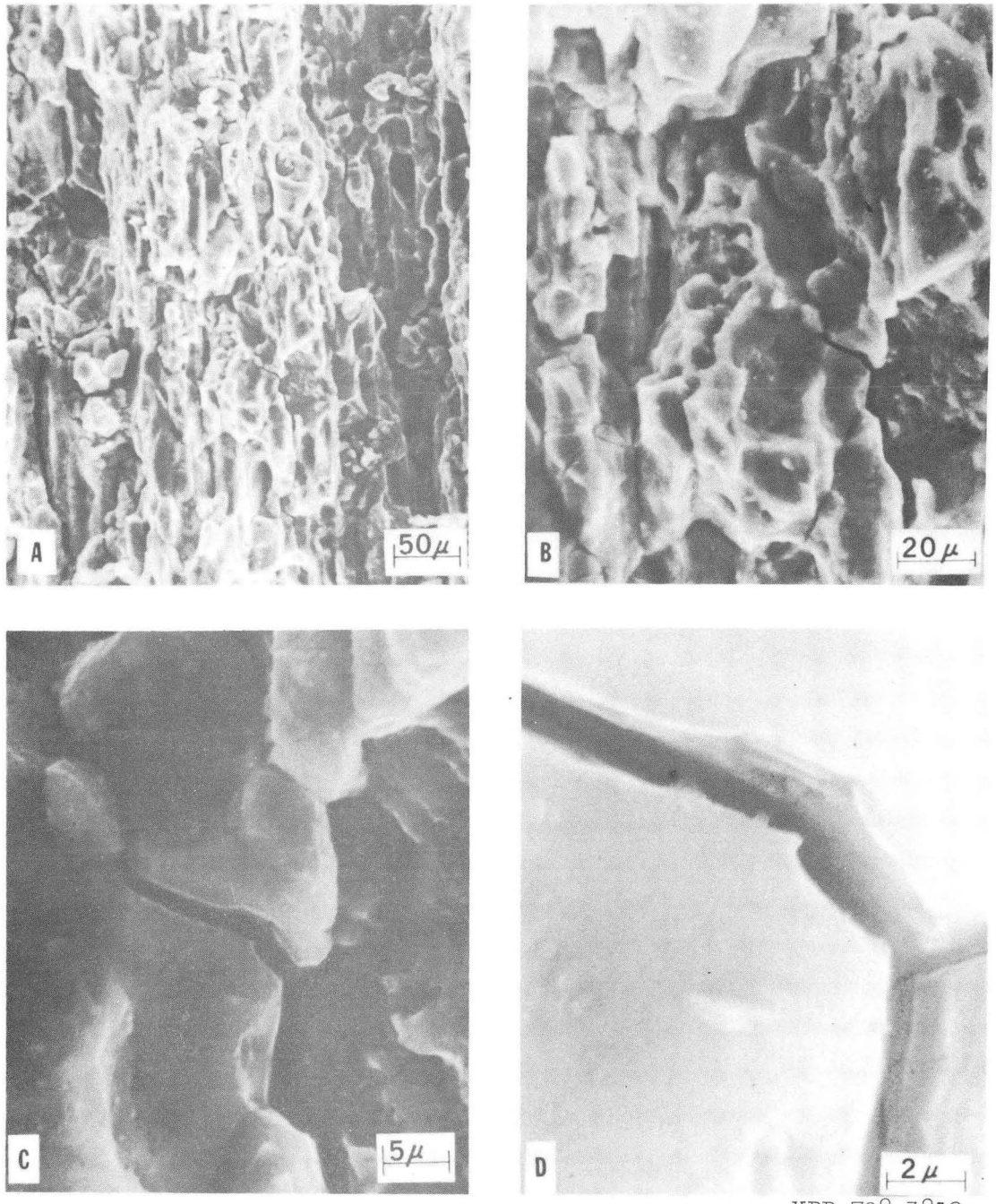

XBB 708-3812

Figure 23

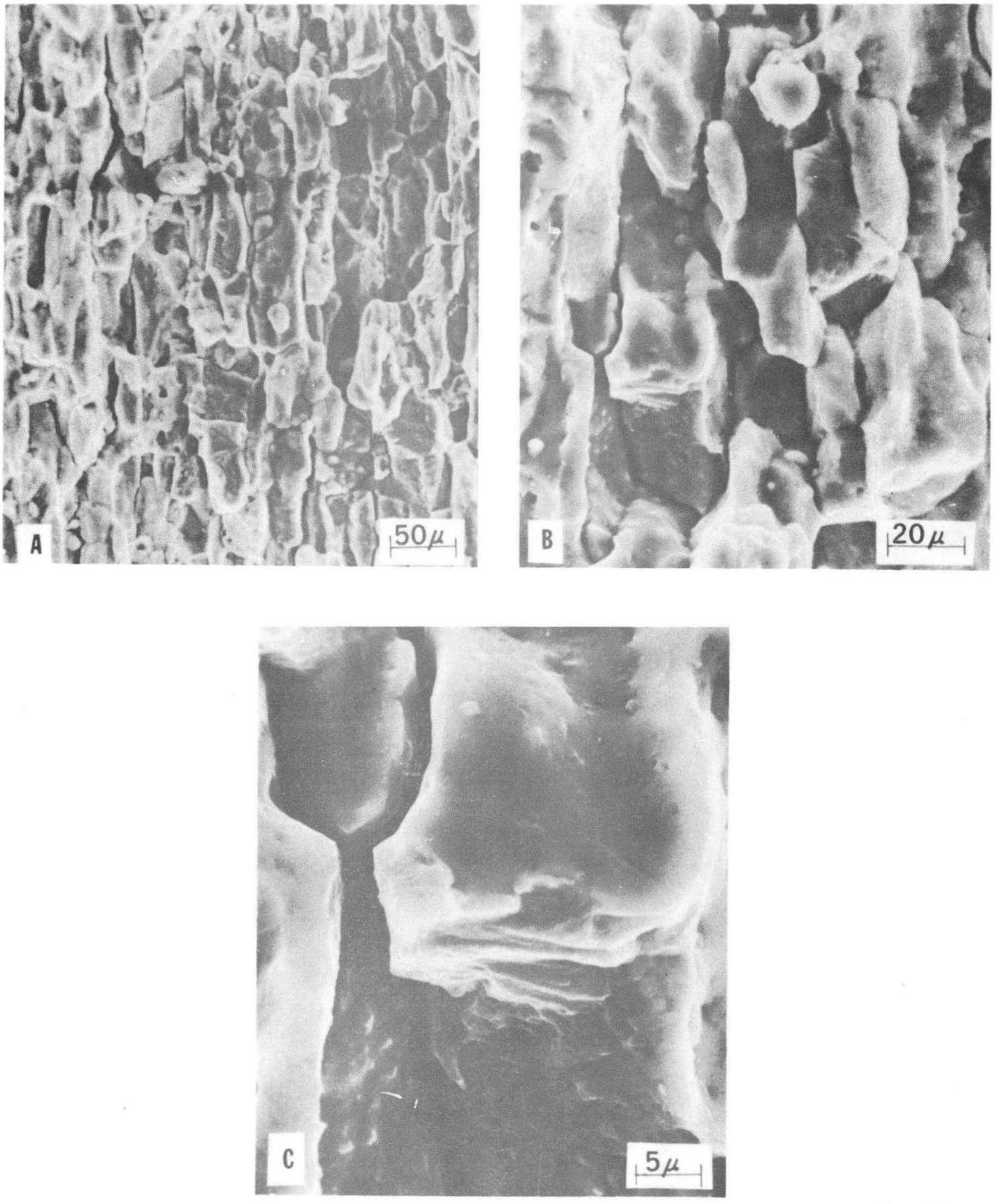

XBB 708-3819

Figure 24

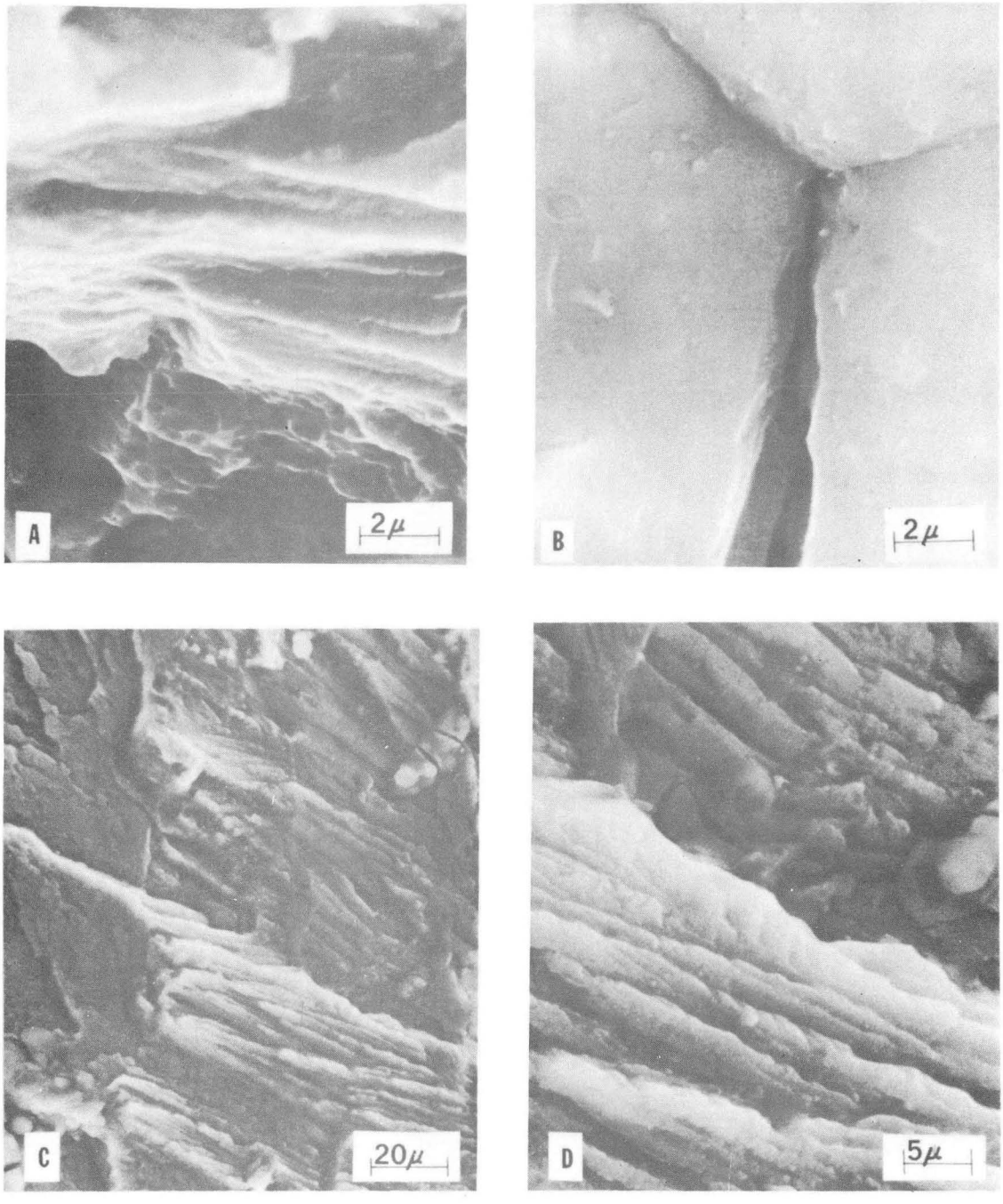

XBB 708-3823

Figure 25

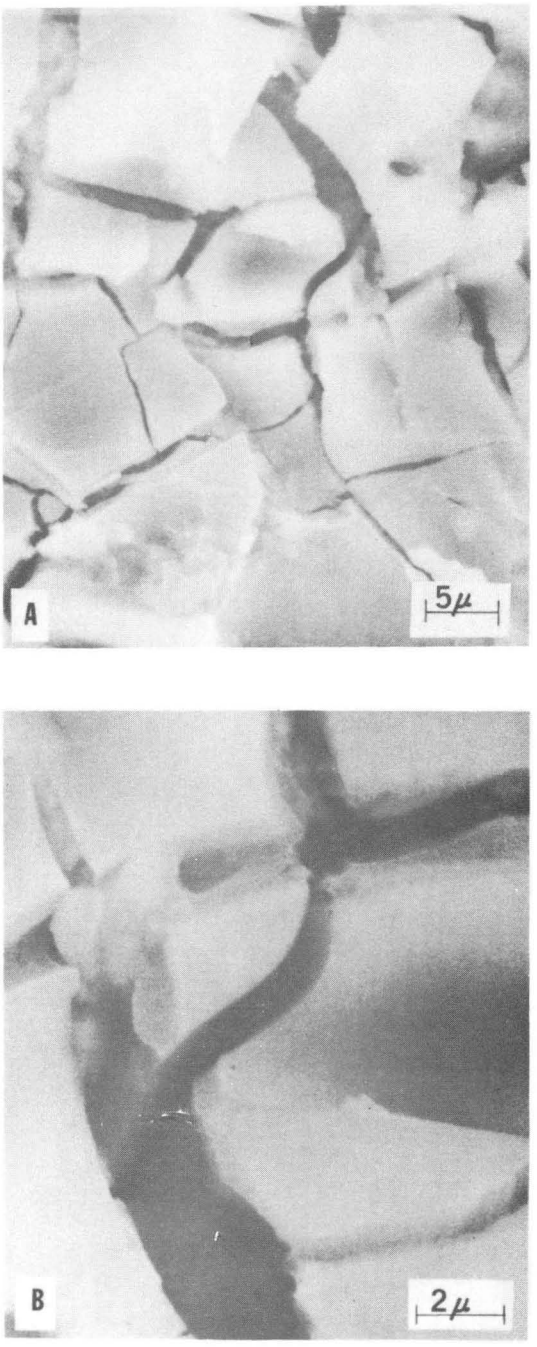

XBB 708-3821

Figure 26

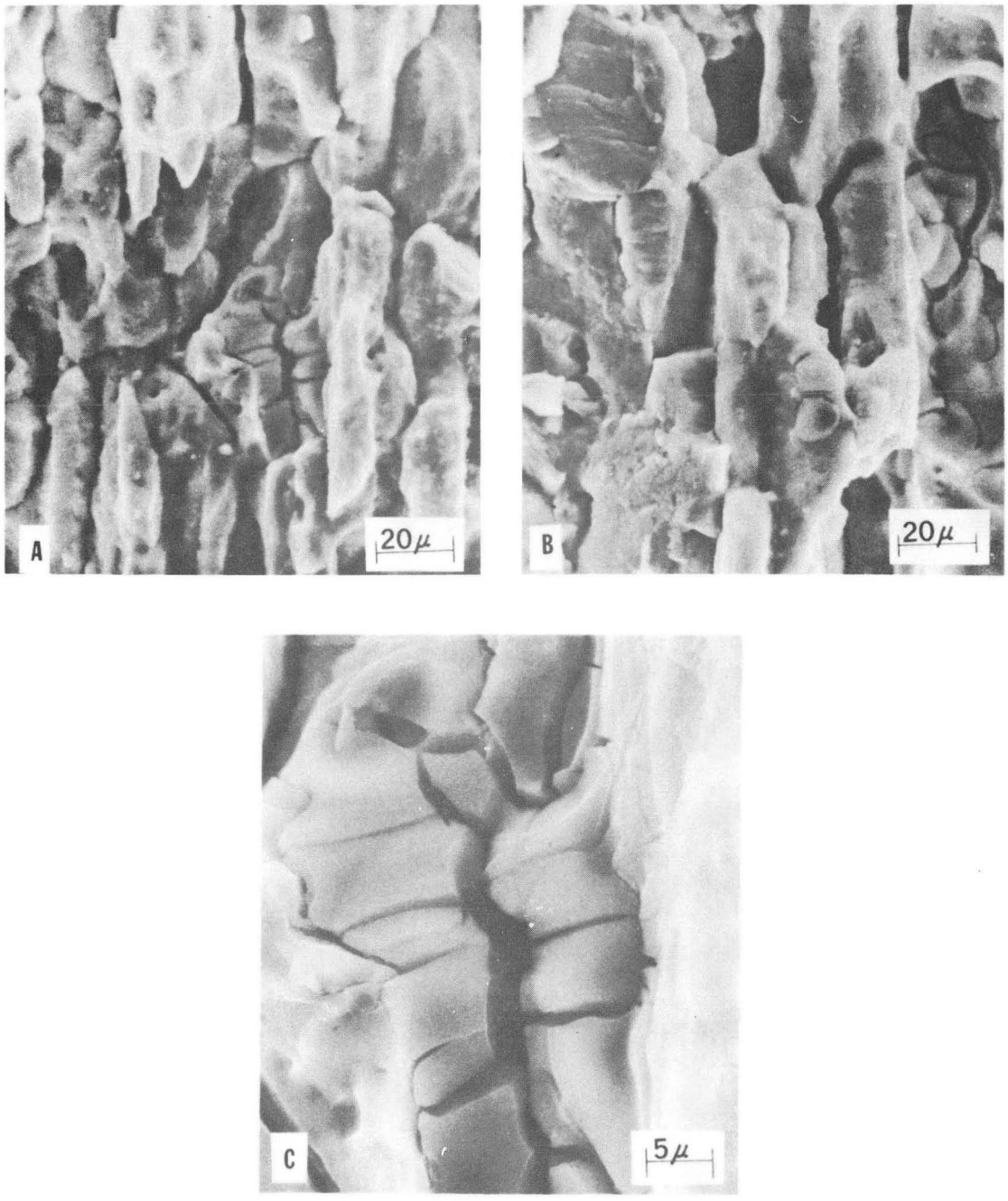

XBB 708-3816

Figure 27

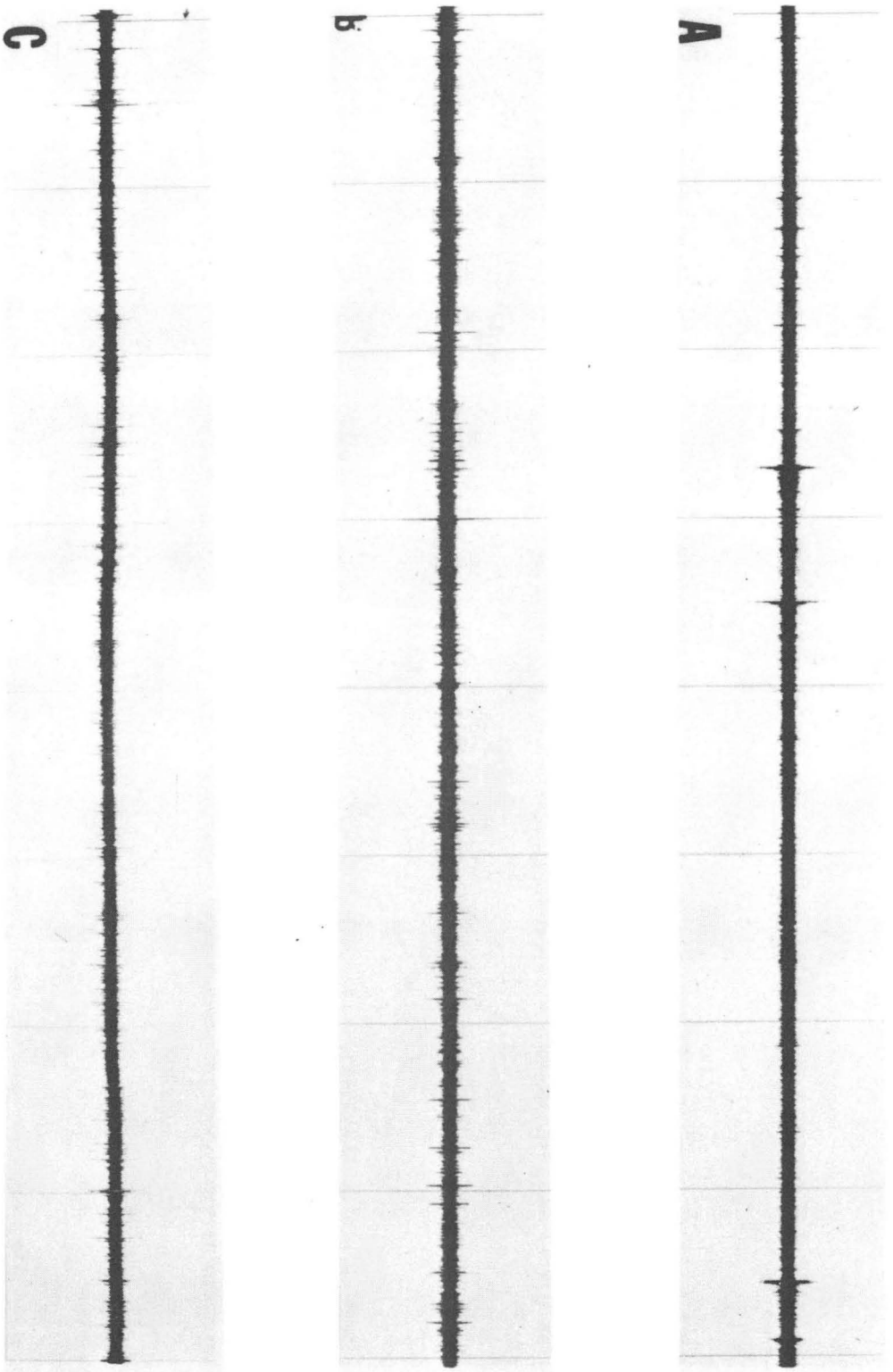

Figure 28

XBB 708-3808

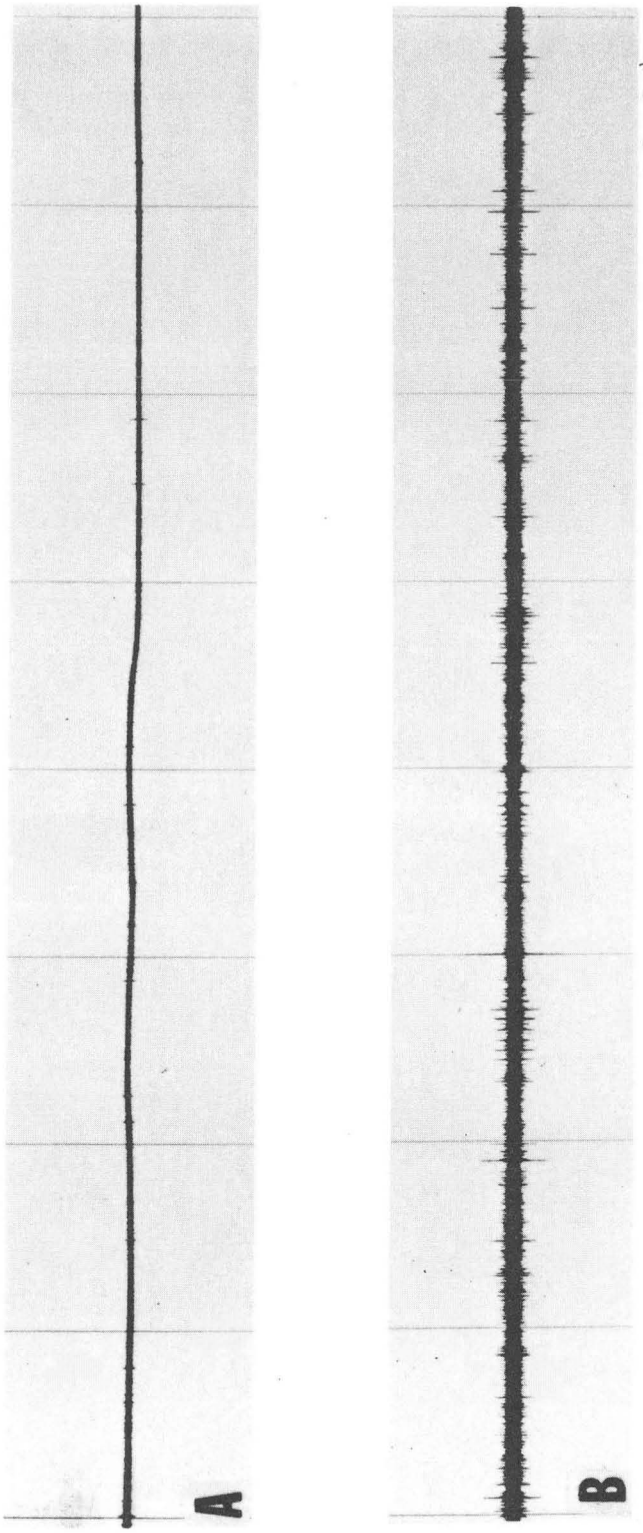

XBB 708-3804

Figure 29

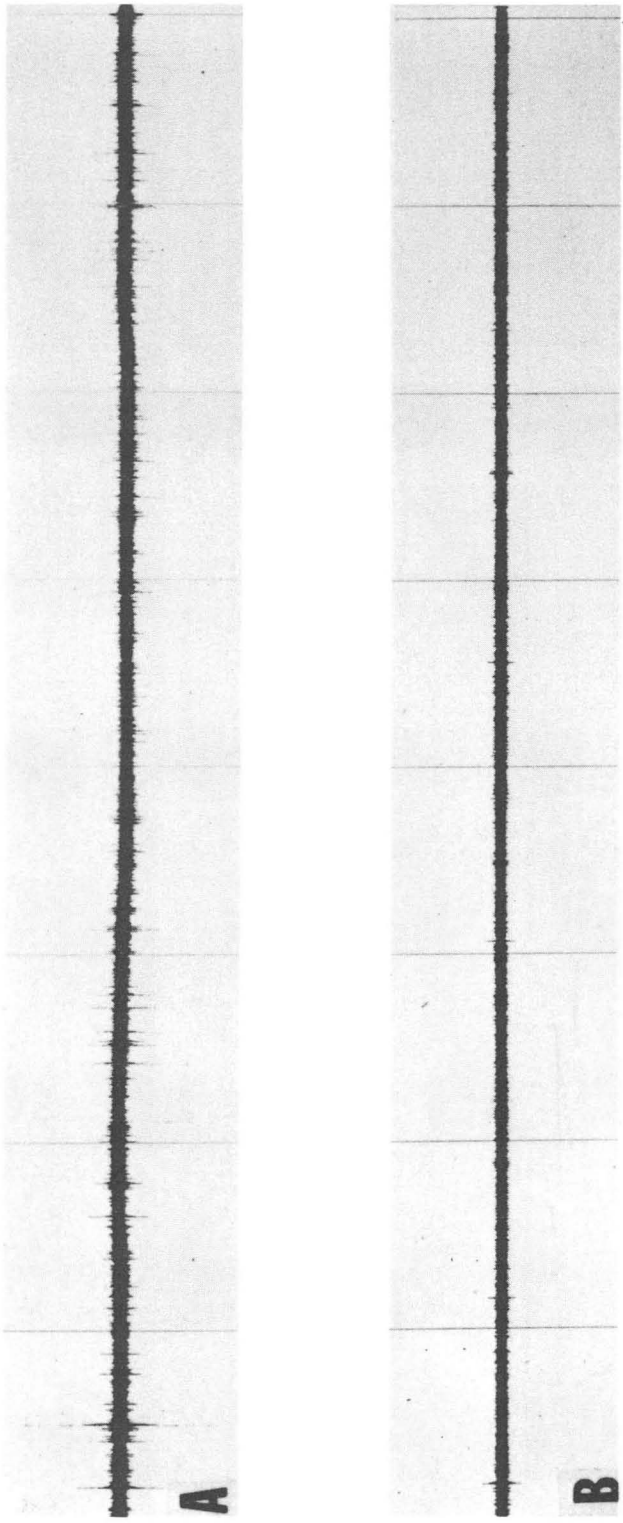

XBB 708-3805

Figure 30

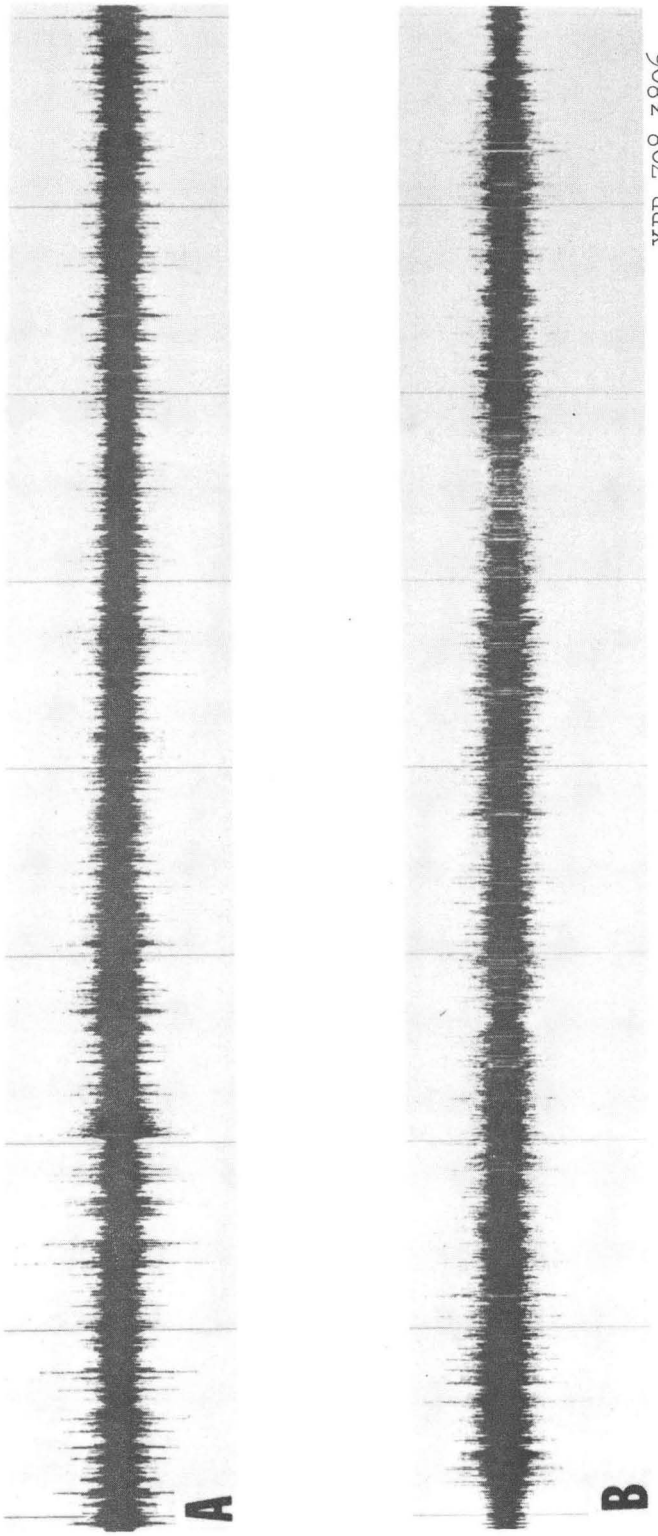

XBB 708-3806

Figure 31

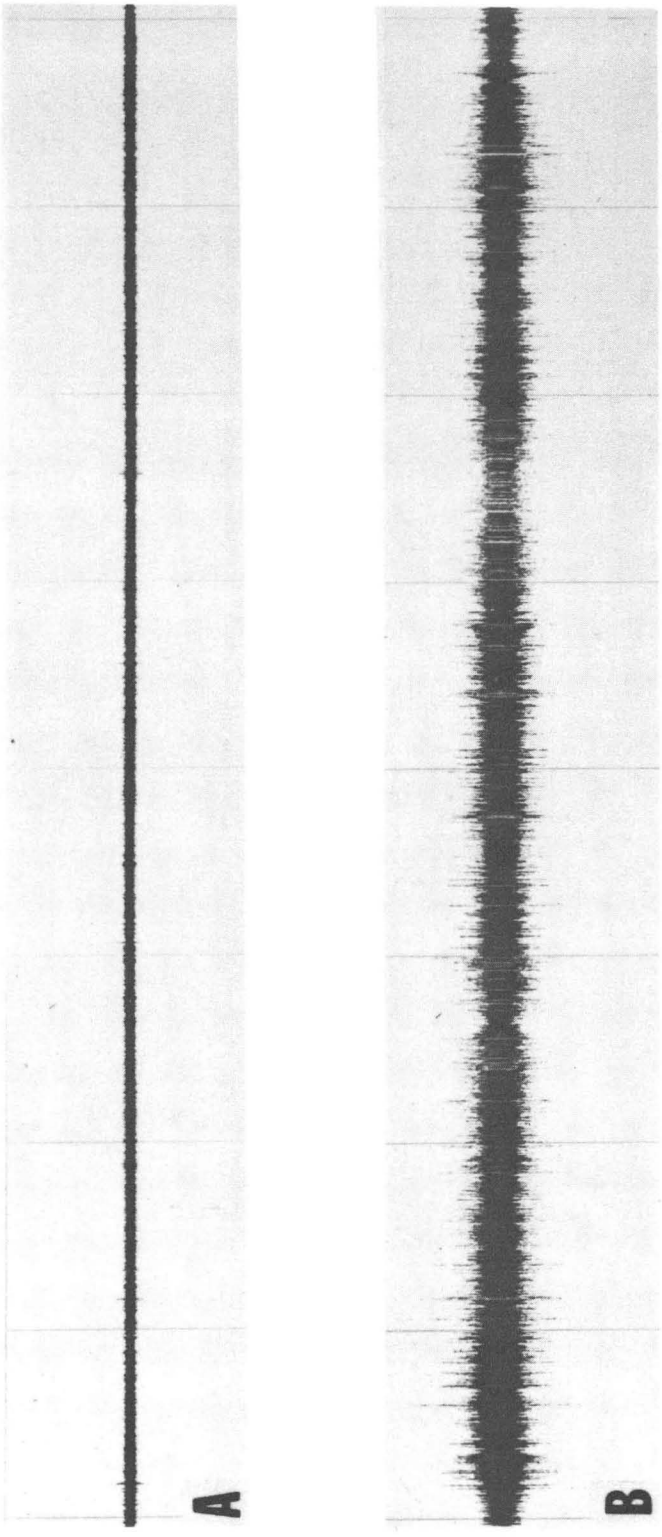

XBB 708-3807

Figure 32

LEGAL NOTICE

TECHNICAL INFORMATION DIVISION
LAWRENCE RADIATION LABORATORY
UNIVERSITY OF CALIFORNIA
BERKELEY, CALIFORNIA 94720